

Lawrence Berkeley National Laboratory

LBL Publications

Title

p - p Elastic Scattering in the Energy Range 300 to 700 MeV

Permalink

<https://escholarship.org/uc/item/9wm328cp>

Authors

Ogden, Philip M

Hagge, Donald E

Helland, Jerome A

et al.

Publication Date

1964-08-01

Copyright Information

This work is made available under the terms of a Creative Commons Attribution License, available at <https://creativecommons.org/licenses/by/4.0/>

University of California
Ernest O. Lawrence
Radiation Laboratory

π - p ELASTIC SCATTERING IN THE ENERGY RANGE
300 TO 700 MeV

TWO-WEEK LOAN COPY

*This is a Library Circulating Copy
which may be borrowed for two weeks.
For a personal retention copy, call
Tech. Info. Division, Ext. 5545*

Berkeley, California

DISCLAIMER

This document was prepared as an account of work sponsored by the United States Government. While this document is believed to contain correct information, neither the United States Government nor any agency thereof, nor the Regents of the University of California, nor any of their employees, makes any warranty, express or implied, or assumes any legal responsibility for the accuracy, completeness, or usefulness of any information, apparatus, product, or process disclosed, or represents that its use would not infringe privately owned rights. Reference herein to any specific commercial product, process, or service by its trade name, trademark, manufacturer, or otherwise, does not necessarily constitute or imply its endorsement, recommendation, or favoring by the United States Government or any agency thereof, or the Regents of the University of California. The views and opinions of authors expressed herein do not necessarily state or reflect those of the United States Government or any agency thereof or the Regents of the University of California.

UNIVERSITY OF CALIFORNIA

Lawrence Radiation Laboratory
Berkeley, California

AEC Contract No. W-7405-eng-48

π - p ELASTIC SCATTERING IN THE ENERGY RANGE
300 TO 700 MeV

Philip M. Ogden, Donald E. Hagge, Jerome A. Helland,
Marcel Banner, Jean-François Detoeuf, and Jacques Teiger

August 12, 1964

π -p ELASTIC SCATTERING IN THE ENERGY RANGE
300 TO 700 MeV*

Philip M. Ogden,[†] Donald E. Hagge,[†] and Jerome A. Helland^{**}

Lawrence Radiation Laboratory
University of California
Berkeley, California

and

Marcel Banner, Jean-François Detoeuf, and Jacques Teiger^{††}

Centre d'Etudes Nucléaires
Saclay, France

August 12, 1964

ABSTRACT

Differential cross sections for elastic π -p scattering were measured at eight energies for positive pions and seven energies for negative pions. Energies ranged from 310 to 650 MeV. These measurements were made at the 3-GeV proton synchrotron at Saclay, France. A beam of pions from an internal BeO target was directed into a liquid hydrogen target. Fifty-one scintillation counters and a matrix-coincidence system were used to measure simultaneously elastic events at 21 angles and charged inelastic events at 78 π -p angle pairs. Events were detected by coincidence of pulses indicating the presence of an incident pion, scattered pion, and recoil proton, and the results were stored in the memory of a pulse-height analyzer. Various corrections were applied to the data and a least-squares fit was made to the results at each energy. The form of the fitting function was a power series in the cosine of the center-of-mass angle of the scattered pion. Integration under the fitted curves gave values for the total elastic cross sections (without charge exchange). The importance of certain angular-momentum states is discussed. The π^- -p data are consistent with a D_{13} resonant state at 600 MeV, but do not necessarily require such a resonant state.

I. INTRODUCTION

This experiment constitutes a portion of an extensive study of the phenomenology of the π -N interaction at energies above that of the well-known $(3/2, 3/2)$ resonance occurring at a pion kinetic energy of 195 MeV (≈ 1236 MeV total c. m. energy for the π -N system). Differential and total elastic cross sections were measured for the interactions $\pi^+ p \rightarrow \pi^+ p$ and $\pi^- p \rightarrow \pi^- p$. In Fig. 1 we see plots of the total cross sections for $\pi^+ - p$ and $\pi^- - p$ scattering as functions of the lab kinetic energy of the pion. The vertical lines represent the energies at which the measurements of this experiment were made; they are 310, 370, 410, 450, 490, 550, 600, and 650 MeV. The $\pi^+ - p$ interaction was studied at all eight energies; for $\pi^- - p$ 310 MeV was omitted.

Many experiments have been performed at energies below 310 MeV. This low-energy region, dominated by the $(3/2, 3/2)$ resonant state, is understood quite well. Recent extensive measurements at 310 MeV by Foote et al., Hill, Rugge, and Vik have given a fairly complete description of the π -N interaction at that energy.¹ Also, considerable information is available in the energy range from 550 to 1600 MeV from the experiments of Helland et al., Wood et al., and Eandi.²

The purpose of this experiment was to give information in the 300- to 650-MeV region in an attempt to bridge the gap in the existing data. Several experiments have been performed in this region.³ However, the statistical accuracy of those measurements is quite poor in general, and in several cases the gap in energy between measurements is quite large.

In the study of the π -N interaction it is of interest to know the role of the various angular-momentum states. Such information can be obtained from a partial-wave analysis, in which the scattering is defined by a set of phase shifts.

As the energy is increased, a partial-wave analysis becomes more difficult because of the large number of angular-momentum states that become important. Furthermore, when inelastic processes become possible, the phase shifts become complex quantities and this results in a doubling of the number of necessary parameters. For these reasons a partial-wave analysis at a single energy produces many possible solutions. It is hoped that, by requiring that the phase shifts be continuous functions of energy, most solutions can be eliminated.

In order to apply the restrictions of energy continuity, it is necessary to have a closely spaced network of accurate data. Thus, we realize the importance of data in the 300-to-650-MeV. range in connecting the low-energy data with the high-energy data.

II. EXPERIMENTAL PROCEDURE AND EQUIPMENT

A. Procedure

A plan view of the experiment is shown in Fig. 2. Positive and negative pions were produced in a BeO target inside Saturne, the Saclay proton synchrotron. By means of a magnetic optical system, a beam of pions with the desired charge was momentum-analyzed and focused on a liquid hydrogen target. Four scintillation counters were used to monitor the beam. Because protons in the positive pion beam had a longer time of flight than pions, response of the counting system to protons was eliminated electronically. Response to electrons and a portion of the muons in the beam was eliminated with a gas Cerenkov counter. Cases in which two beam particles were too close together in time were eliminated electronically.

Scattered pions and their associated recoil protons emerging from the liquid hydrogen target were detected with an array of 46 scintillation counters. Elastic-scattering events were detected by a coincidence of pulses indicating the presence of the incident pion, scattered pion, and recoil proton. Geometric restrictions requiring that the event be coplanar or nearly coplanar and at proper pion and proton angles minimized the inelastic contamination. By measuring inelastic events in the region near the elastic events, a correction was determined for the elastic channels. Elastic events at 21 scattering angles and charged inelastic events at 78 π -p "off-elastic angle" pairs were simultaneously measured and stored in the memory of a pulse-height analyzer. At the end of each run the data in the memory were simultaneously punched on IBM cards and typed by an electric typewriter.

B. Beam Design and Hydrogen Target

The internal Saturne beam of 3-GeV protons was caused to impinge upon a BeO target. As shown in Fig. 2, a symmetric optical system consisting of two triplet quadrupole magnets (Q_1 and Q_2) and two bending magnets (B_1 and B_2) conducted particles of the proper charge and momentum from the internal target to a position and momentum focus at the hydrogen target. A lead (Pb) collimator was incorporated at the intermediate focus to define a spread of $\pm 3\%$ in the beam momentum.

The liquid hydrogen target was 10.3 cm long and was similar to the target described in reference 2a.

C. Scintillation and Cerenkov Counters

Four scintillation counters and a Cerenkov counter were used to monitor the beam (see Fig. 2). Counters M_1 and M_3 were beam-defining counters, M_1 being at the intermediate image and M_3 being 15 cm in front of the

hydrogen target. Counters M_{1A} and M_2 were large counters designed to detect all the beam particles. A coincidence of signals from M_1 , M_2 , and M_3 formed the basis of the beam monitor system. The signal from M_{1A} and a second signal from M_2 were used in the double-pulse-rejection system (discussed in reference 2a).

In order to reject electronically the electrons and a portion of the muons, a gaseous ethylene Cerenkov counter C was placed near the intermediate image. Ethylene was chosen because at easily attainable pressures it has an index of refraction in the proper range to distinguish between muons and pions at the energies of this experiment. At 310 MeV an absolute pressure of 42.5 kg/cm^2 was required. The Cerenkov counter is described in reference 4.

The array of 46 scintillation counters used to detect scattered particles is shown schematically in Fig. 3. The 21 π counters were placed to the right of the beam at various lab angles between 25 and 153 deg. Their purpose was to detect scattered pions.

The solid-angle region available to protons conjugate to the pions detected by the π counters was covered by 25 overlapping counters called ρ counters. The ρ counters were combined in 21 groups, each group containing from three to seven counters. Such a group, called a P counter, detected all protons conjugate to the corresponding π counter. The ρ counter signals for a given group were added electronically. The way in which the ρ counters were combined was different for each energy of the incident pion beam.

The counter S_0 , shown partly around the hydrogen target in Fig. 3, was arranged so as to be missed by the pions in the beam but to be traversed by any pion scattered from the target into a π counter.

D. Electronic Apparatus

The electronic apparatus consisted of three systems: the beam-monitor system, the matrix-coincidence system, and the core storage system. These systems were very similar to those used in the experiment by Helland et al.^{2a} Two differences should be noted: (a) Changes were made in the beam-monitor system to improve its frequency response and reliability. (b) A 100-channel core storage was used instead of the original 64-channel core storage. The matrix-coincidence system was modified to adapt to the larger core storage. These changes made possible an increase in the number of inelastic channels from 42 to 78.

III. DATA ANALYSIS

Data were reduced and corrections applied in a manner similar to that of Helland et al.^{2a} Two exceptions were: (a) The necessity of a correction for electron contamination in the beam was eliminated by the use of the Cerenkov counter C. (b) Muon-contamination corrections were smaller than in the experiment of Helland et al., because of the use of the Cerenkov counter. The muon correction in this experiment ranged from 2.25% at 650 MeV to 4.1% at 310 MeV.

IV. RESULTS

A. Differential Cross Sections

The results of the differential-cross-section measurements and the associated errors in standard deviations are given in Tables I through VIII. The values given for $\cos \theta^* = 1.0$ are theoretical values obtained from the optical theorem and dispersion relations. The dispersion-relations calculation is that of Cence, Cheng, and Chiu.⁵

B. Least-Squares Fitted Curves

The curve of the form

$$\frac{d\sigma(\theta^*)}{d\Omega} = \sum_{n=0}^N a_n \cos^n \theta^* \quad (4)$$

was least-squares fitted to the data.⁶ The coefficients a_n were determined by the least-squares calculation. The error matrix of the least-squares fit was used to determine the errors in the coefficients.

The differential cross-section data and fitted curves are plotted in Figs. 4 through 7. The dispersion-relations points were used in making the fits. For π^+ -p, a fourth-order fit--i. e., $N=4$ --was used at all energies. For π^- -p, a fourth-order fit was used at 370 and 410 MeV, and a fifth-order fit at energies 450 MeV and above.

The coefficients and their errors are listed for each energy and charge in Tables IX and X. They are also plotted as a function of energy in Figs. 8 and 9.

Several criteria were considered in choosing the order of fit. One criterion was that if a given order were required at a certain energy, no lower order was ever chosen at a higher energy. This corresponds to the principle that as the energy increases, the number of partial waves taking part in the scattering should not decrease.

An interesting test was made by comparing the fits obtained with and without the dispersion-relations point. In almost every case, the two fits for the chosen order were nearly identical.

An important consideration was the standard χ^2 test. The goodness-of-fit parameter, $(\chi^2/d)^{1/2}$, for which d is the number of degrees of freedom, was calculated for each order. The chosen order was the lowest one for which an increase in the order gave little change in the goodness-of-fit parameter. Except for a few cases in which the other previously

mentioned criteria indicated strongly that a higher order was needed, the χ^2 test determined the order of fit. The goodness-of-fit parameter, the order of fit, and the number of degrees of freedom for each energy are listed in Table XI for $\pi^+ - p$ and Table XII for $\pi^- - p$.

C. Total Elastic Cross Sections

By integrating under the fitted differential cross-section curves, measurements of the total elastic cross section were obtained. These values and their errors are listed in Table XIII and plotted as a function of energy in Fig. 10.

V. DISCUSSION

A. Partial-Wave Equations

In the study of the pion-nucleon interaction, it is of interest to know how the various angular-momentum states participate in the scattering. Particularly, one would like to know what states, if any, are dominant. One approach to this problem is to examine the behavior, as a function of energy, of the coefficients of a cosine-power-series expansion of the differential cross section.

The partial-wave expansion of the differential cross section for a spinless particle (pion) and a spin-1/2 particle (proton) is

$$\frac{d\sigma(\theta^*)}{d\Omega^*} = \left| \sum_{\ell=0}^{\infty} [(\ell+1)A_{\ell}^+ + \ell A_{\ell}^-] P_{\ell}(\cos \theta^*) \right|^2 + \left| \sum_{\ell=1}^{\infty} (A_{\ell}^+ - A_{\ell}^-) P_{\ell}^1(\cos \theta^*) \right|^2. \quad (2)$$

The index ℓ represents the orbital angular-momentum state, and the + and - superscripts indicate that the total angular momentum J is $\ell + 1/2$ or $\ell - 1/2$, respectively. The functions $P_{\ell}(\cos \theta^*)$ and $P_{\ell}^1(\cos \theta^*)$ are

respectively the Legendre polynomial and the first associated Legendre polynomial of order l . The partial-wave scattering amplitude A_l^\pm can be written as a function of the real part of the phase shift δ_l^\pm , the absorption parameter η_l^\pm , and the c. m. wave number k :

$$A_l^\pm = [\eta_l^\pm \exp(2i\delta_l^\pm) - 1]/2ik. \quad (3)$$

If the summations in Eq. (2) are cut off at a value l_{\max} , that expression can be expanded and the terms recombined in the form

$$\frac{d\sigma(\theta^*)}{d\Omega^*} = \sum_{n=0}^{2l_{\max}} a_n \cos^n \theta^*. \quad (4)$$

This expansion relates the coefficients a_n to the partial-wave amplitudes. (See Eq. 16 of reference 2a.)

B. Interpretation of π^+ -p Results

The π^+ -p coefficients are plotted vs energy in Fig. 8. The smooth behavior of the coefficients indicates that little of interest is occurring in the $T=3/2$ state in this energy range. Below 300 MeV we know that the scattering is dominated by the P_{33} state, resonant at about 200 MeV. The smooth decrease in a_0 , a_1 , and a_2 in going from 300 to 700 MeV can easily be recognized as a result of the decreasing importance of the P_{33} state.

One observation regarding the D-wave phases can be made from a consideration of the coefficient a_4 . Since a fifth- or higher-order fit was not needed, we are fairly confident that F waves can be neglected. With this assumption, we have

$$a_4 = 45 \operatorname{Re}(D_{33}^* D_{35}) + (45/4) |D_{35}|^2. \quad (5)$$

From Fig. 8 we see that a_4 is negative. Since the second term in Eq. (5)

is positive definite, the first term must be negative. This implies that the D_{33} and D_{35} phases have opposite signs.

C. Interpretation of π^- -p Results

Next, let us consider the more complicated π^- -p situation. The presence of both isotopic spin states makes the interpretation of the coefficients difficult. However, we have seen that the $T=3/2$ states are in general of small amplitude and slowly varying in this energy range.

The π^- -p coefficients are plotted vs energy in Fig. 20. Considerable structure is apparent in the region around 600 MeV. This structure appears to be associated with peaks in both the total cross section (Fig. 1) and the total elastic cross section (Fig. 10).

Several explanations have been given for the 600-MeV enhancement. Peierls, on the basis of photoproduction measurements, ascribed the enhancement to a resonance in the D_{13} state.⁷ Bareyre et al. have recently reported evidence that a D_{13} resonance is not sufficient, and that a resonance in either the S_{11} or P_{11} state may occur at about 430 MeV in addition to a D_{13} resonance at 600 MeV.⁸ Further suggestion of two resonant states is given by the recent partial-wave analysis by Roper.⁹

Neither a P_{11} nor a D_{13} resonance fits in the scheme of the Regge-pole hypothesis.¹⁰ Furthermore, the nucleon itself can be considered as a P_{11} π -N state, and one would not expect two distinct resonances with identical quantum numbers. Such theoretical difficulties and various other considerations have led many to believe that the 600-MeV enhancement is a result of inelastic processes. Ball and Frazer have pointed out that a rapidly increasing inelastic cross section may give rise to a peak in the elastic cross section.¹¹ Such a behavior could also be associated with certain prominent angular-momentum states.

A few general remarks about resonances are in order. The Breit-Wigner resonance theory predicts for an elastic resonant amplitude the form¹²

$$kA = \Gamma_{el} / [2(E_R - E) - i\Gamma]. \quad (6)$$

Here, Γ_{el} and Γ are the elastic and total widths of the resonance. The total c.m. energy is E and the resonant energy is E_R . It is convenient to introduce the notation of Watson et al.,¹³

$$x = \Gamma_{el} / \Gamma \quad (7)$$

and

$$\epsilon = (2/\Gamma)(E_R - E). \quad (8)$$

In terms of these symbols,

$$kA = x / (\epsilon - i). \quad (9)$$

If the polar form of kA is used, that is,

$$kA = |kA| \exp(i\theta), \quad (10)$$

one can show

$$\epsilon = \cot \theta \quad (11)$$

and

$$|kA| = x \sin \theta. \quad (12)$$

Thus, if the elasticity x is constant, the amplitude kA lies on a circle of radius $x/2$, as shown in Fig. 11.

In order to assess the compatibility of the data of this experiment with a D_{13} resonance, we shall assume that a D_{13} resonance with a Breit-Wigner form is present and attempt to fit the energy variation of the $\pi^- - p$ coefficients. Certain reasonable assumptions will be made about the other states involved. The accuracy of the fits will determine the compatibility of the data with the assumptions.

In this rough analysis we shall neglect the effects of the states whose amplitudes we would expect to be small--namely, the P_{13} , D_{33} , D_{35} , and F_{35} states, and all states with total angular momentum $J > 5/2$. Experiments at higher energies have indicated that the F_{15} state is resonant and the D_{15} amplitude large (or vice versa) at about 900 MeV.² We shall assume an F_{15} resonance at 900 MeV with a Breit-Wigner form. A Breit-Wigner form for the P_{33} resonance will also be used, the width being such as to agree at 340 MeV with the partial-wave analysis by Foote et al.^{1b} The parameters α , Γ , and E_R , which we shall use for the P_{33} , D_{13} , and F_{15} resonances, are given in Table XIV. Those for the D_{13} and F_{15} states were either taken directly from or estimated from the work of Omnes and Valladas.¹⁴ These parameters were chosen somewhat arbitrarily and should not be taken too seriously.

The real and imaginary parts of the resonant amplitudes are plotted vs energy in Fig. 12. On the low-energy side of the D_{13} and F_{15} resonances, multiplicative factors were put in to bring the amplitudes to zero. This was necessary because of the simplifying assumption that the Γ 's were constant.

The behavior assumed for the $S_{1/2}$, $P_{1/2}$, and D_{15} states is shown in Fig. 13. Motivation for the assumptions made is given in the ensuing paragraphs.

Let us now consider the coefficient a_0 . The $|D_{3/2}|^2$ term gives a positive peak at 600 MeV, as shown in Fig. 14. From Fig. 9 we see that no such peak appears in a_0 . However, if we assume that the real part of the $S_{1/2}$ amplitude is negligibly small and that the imaginary part is constant at a value 0.27, the $S_{1/2}D_{3/2}$ interference term cancels the effect of the $|D_{3/2}|^2$ term. The $S_{1/2}D_{3/2}$ term is shown with the $|D_{3/2}|^2$ term in Fig. 14. The assumption of a pure imaginary S-wave amplitude is not unreasonable in view of the fact that one would expect inelastic scattering to be most important in the low-angular-momentum states. Furthermore, since the $\pi^- - p$

amplitude is a combination of two amplitudes, it could be pure imaginary even though the phase shifts for the individual isotopic spin states may be pure real. If $2\text{Re}S_{11} = -\text{Re}S_{31}$, the resultant $S_{1/2}$ amplitude for π^-p is pure imaginary.

The same two terms, $|D_{3/2}|^2$ and $S_{1/2}D_{3/2}$, which have opposite signs in a_0 , have the same sign in a_2 and combine to produce a large peak, as shown in Fig. 15. This is consistent with the large positive peak in a_2 shown in Fig. 9.

The general trend in the coefficient a_4 appears to be consistent with a $D_{3/2}D_{5/2}$ interference for which the $D_{5/2}$ amplitude has the form shown in Fig. 13. The contribution to a_4 from this term is plotted in Fig. 16.

The contribution to a_3 from $P_{3/2}D_{3/2}$ interference is shown in Fig. 17 together with that from $D_{5/2}F_{5/2}$ interference. These two terms give the proper trend in a_3 .

The states discussed so far do not give a good prediction for the coefficient a_1 . Both the $P_{3/2}D_{3/2}$ and $D_{5/2}F_{5/2}$ terms give little contribution to a_1 at 600 MeV, as shown in Fig. 18. However, a 2-mb peak in a_1 is indicated by the data in Fig. 9. The only other state that could interfere with the $D_{3/2}$ state and contribute to a_1 is the $P_{1/2}$ state. If we assume, as we did for the $S_{1/2}$, that the $P_{1/2}$ amplitude is pure imaginary and constant, the $P_{1/2}D_{3/2}$ contribution to a_1 is as shown in Fig. 18. Furthermore, the $P_{1/2}D_{3/2}$ interference term does not contribute to any other coefficient.

Thus one can see the motivation for choosing the forms of the amplitudes given in Figs. 12 and 13. Using these amplitudes and considering all the terms that contribute to each coefficient, we obtain the behavior of the coefficients shown in Fig. 19. The data of this experiment and the 698-MeV data of Helland et al.^{2a} are also plotted in Fig. 19.

One can see that the agreement between the data and the predictions is fairly good in view of the many simplifying assumptions made. This does not prove the existence of a resonance in the D_{13} state, but shows that the data appear to be consistent with a D_{13} resonance.

The amplitudes chosen to fit the coefficients of the angular distributions can also be used to predict the polarization of the recoil proton. In Fig. 20 the predicted polarizations for 523, 572, and 689 MeV are plotted with the data of Eandi.^{2d} Although the agreement at 523 MeV is not very good, the predictions for 572 and 589 MeV fit the data very well.

In regard to the evidence for two resonances in the 400-to-700-MeV region, it can only be said that in this rough analysis the necessity of a second resonance was not apparent.

In summary, we can say that the D_{13} state rises to prominence in the energy region from 400 to 700 MeV. Furthermore, it appears that the π^- -p differential cross section data are consistent with a D_{13} phase shift that passes through 90 deg. However, an alternative explanation cannot be ruled out. Because of the importance of inelastic processes, the D_{13} resonance, if indeed it may be called a resonance, may be of a nature fundamentally different from that of a bound-state type of resonance, associated with a Regge pole. Further investigation will be necessary to resolve these uncertainties. Accurate polarization and charge-exchange measurements should aid in a better understanding of this problem.

ACKNOWLEDGMENTS

The authors would like to acknowledge the assistance of Mr. Jean Hamel and Mr. Larry Scott in the performance of the experiment. Thanks are also due Professor Burton J. Moyer and Professor A. C. Helmholtz for their many helpful suggestions and their continued interest in the experiment.

FOOTNOTES AND REFERENCES

- *This work was done under the auspices of the U. S. Atomic Energy Commission and the French Commissariat a l'Energie Atomique.
- *Present address: Seattle Pacific College, Seattle, Washington.
- †Present address: Goddard Space Flight Center, Greenbelt, Maryland.
- **Present address: University of California, Los Angeles, California.
- ††Assigned to Centre d'Etudes Nucléaires by the University of Caen, Caen, France.

1. (a) J. H. Foote, O. Chamberlain, E. H. Rogers, H. M. Steiner, C. E. Wiegand, and T. Ypsilantis, *Phys. Rev.* 122, 948 (1961);
(b) J. H. Foote, O. Chamberlain, E. H. Rogers, and H. M. Steiner, *Phys. Rev.* 122, 959 (1961);
(c) H. R. Rugge and O. T. Vik, *Phys. Rev.* 129, 2300 (1963);
(d) O. T. Vik and H. R. Rugge, *Phys. Rev.* 129, 2311 (1963);
(e) Roger Hill, Pion-Nucleon Scattering at 310 MeV: Neutron Polarization in $\pi^- + p \rightarrow \pi^0 + n$ and Phase Shift Analysis (Ph. D. Thesis), Lawrence Radiation Laboratory Report UCRL-11140, Dec. 1963 (unpublished).
2. (a) J. A. Helland, T. J. Devlin, D. E. Hagge, M. J. Longo, B. J. Moyer, and C. D. Wood, *Phys. Rev.* 134, B1062; 134, B1079 (1964);
(b) C. D. Wood, T. J. Devlin, J. A. Helland, M. J. Longo, B. J. Moyer and V. Perez-Mendez, *Phys. Rev. Letters* 6, 481 (1961);
(c) Richard D. Eandi, Polarization of Recoil Protons in Pion-Proton Elastic Scattering at 523, 572, and 689 MeV (Ph. D. Thesis), Lawrence Radiation Laboratory Report UCRL-10629, March 1963 (unpublished).

3. (a) M. E. Blevins, M. M. Block, and J. Leitner, Phys. Rev. 112, 1287 (1958);
(b) R. R. Crittenden, J. H. Scandrett, W. D. Shephard, W. D. Walker, and J. Ballam, Phys. Rev. Letters 2, 121 (1959);
(c) L. K. Goodwin, R. W. Kenney, and V. Perez-Mendez, Phys. Rev. 122, 655 (1961);
(d) F. Grard, G. MacLeod, L. Montanet, M. Cresti, R. Barloutaud, C. Choquet, J. Gaillard, J. Heughebaert, A. Leveque, P. Lehman, J. Meyer, and D. Revel, Nuovo Cimento 22, 493 (1964);
(e) E. L. Grigoryev and N. A. Mitin, Soviet Phys. JETP 10, 1123 (1960);
(f) M. Kozodaev, R. Suliaev, A. Fillipov, and Iu. Shcherbakov, Soviet Phys. Doklady 1, 171 (1956);
(g) R. S. Margulies, Phys. Rev. 100, 1255 (1955);
(h) N. A. Mitin and E. L. Grigoryev, Soviet Phys. JETP 5, 378 (1957);
(i) John I. Shonle, Phys. Rev. Letters 5, 156 (1960);
(j) William J. Willis, Phys. Rev. 116, 753 (1959);
(k) V. G. Zinov and S. M. Korenchenko, Soviet Phys. JETP 11, 794 (1960);
(l) Peter C. A. Newcomb, Phys. Rev. 132, 1283 (1963).
4. J. Duboc, J. Banaigs, and J. F. Detoef, J. Phys. Radium 22, 64A (1961).
5. Robert J. Cence, David A. Cheng, and Charles B. Chiu (Lawrence Radiation Laboratory, Berkeley, California), private communication.
6. P. Cziffra and M. J. Moravcsik, A Practical Guide to the Method of Least Squares, Lawrence Radiation Laboratory Report UCRL-8523 Rev., June 1959 (unpublished).
7. Ronald F. Peierls, Phys. Rev. 118, 325 (1960).
8. P. Bareyre, C. Bricman, G. Valladas, G. Villet, J. Bizard, and J. Seguinot, Phys. Letters 8, 137 (1964).

9. L. David Roper, *Phys. Rev. Letters* 12, 340 (1964).
10. P. Carruthers, *Phys. Rev. Letters* 10, 540 (1963).
11. J. S. Ball and W. R. Frazer, *Phys. Rev. Letters* 7, 204 (1964).
12. J. M. Blatt and V. F. Weisskopf, *Theoretical Nuclear Physics* (John Wiley and Sons, Inc., New York, 1952), p. 400.
13. M. B. Watson, M. Ferro-Luzzi, and R. D. Tripp, *Phys. Rev.* 131, 2248 (1963).
14. R. Omnes and G. Valladas, in *Proceedings of the International Conference on Elementary Particles, Aix-en-Provence, September 1961*, Vol. I, p. 467.

Table I. Differential cross-section data for $T_{\pi} = 310$ MeV.

$\text{Cos}\theta^*$	$\frac{d\sigma(\theta^*)}{d\Omega^*} \text{ (mb/sr)}$ $\pi^+ - p$
1.000	14.090 ± 1.410
0.533	7.102 ± 0.330
0.450	6.391 ± 0.408
0.355	4.775 ± 0.523
0.258	2.722 ± 0.925
0.160	2.910 ± 0.621
0.045	2.071 ± 0.119
-0.067	1.646 ± 0.103
-0.174	1.447 ± 0.104
-0.308	1.402 ± 0.077
-0.472	1.699 ± 0.085
-0.613	2.163 ± 0.104
-0.720	2.818 ± 0.134
-0.800	3.549 ± 0.166
-0.860	3.962 ± 0.205
-0.903	4.214 ± 0.240
-0.946	4.786 ± 0.218

Table II. Differential cross-section data for $T_{\pi} = 370$ MeV.

$\text{Cos } \theta^*$	$d\sigma(\theta^*)/d\Omega^*$ (mb/sr)	
	$\pi^+ - p$	$\pi^- - p$
1.000	10.040 ± 1.000	1.240 ± 0.120
0.584	5.524 ± 0.160	1.305 ± 0.044
0.510	4.845 ± 0.157	1.182 ± 0.052
0.425	4.045 ± 0.212	1.117 ± 0.075
0.328	2.933 ± 0.291	0.899 ± 0.093
0.228	1.918 ± 0.404	0.563 ± 0.114
0.130	1.744 ± 0.585	0.582 ± 0.142
0.014	1.349 ± 0.070	0.581 ± 0.026
-0.098	0.869 ± 0.056	0.447 ± 0.024
-0.204	0.653 ± 0.050	0.448 ± 0.024
-0.336	0.596 ± 0.036	0.389 ± 0.016
-0.496	0.629 ± 0.038	0.429 ± 0.018
-0.632	0.910 ± 0.050	0.506 ± 0.022
-0.735	1.219 ± 0.065	0.650 ± 0.027
-0.811	1.448 ± 0.081	0.740 ± 0.034
-0.868	1.848 ± 0.098	0.823 ± 0.041
-0.908	1.995 ± 0.113	0.933 ± 0.050
-0.949	2.199 ± 0.108	1.000 ± 0.043

Table III. Differential cross-section data for $T_{\pi} = 410$ MeV.

$\text{Cos}\theta^*$	$d\sigma/d\Omega^*$ (mb/sr)	
	$\pi^+ - p$	$\pi^- - p$
1.000	8.150 ± 0.810	1.710 ± 0.170
0.639	5.423 ± 0.116	1.542 ± 0.039
0.571	4.375 ± 0.119	1.383 ± 0.044
0.495	3.841 ± 0.142	1.264 ± 0.065
0.408	3.199 ± 0.218	1.192 ± 0.089
0.310	2.065 ± 0.254	0.928 ± 0.094
0.209	1.342 ± 0.370	0.651 ± 0.125
0.110	1.361 ± 0.363	0.661 ± 0.117
-0.006	0.923 ± 0.052	0.531 ± 0.026
-0.118	0.551 ± 0.038	0.406 ± 0.023
-0.223	0.364 ± 0.036	0.372 ± 0.021
-0.353	0.279 ± 0.025	0.358 ± 0.015
-0.511	0.284 ± 0.029	0.389 ± 0.017
-0.644	0.507 ± 0.036	0.528 ± 0.022
-0.744	0.773 ± 0.044	0.680 ± 0.028
-0.818	0.912 ± 0.055	0.765 ± 0.034
-0.873	1.034 ± 0.066	0.856 ± 0.044
-0.912	1.156 ± 0.077	1.050 ± 0.051
-0.951	1.137 ± 0.070	1.149 ± 0.047

Table IV. Differential cross-section data for $T_{\pi} = 450$ MeV.

$\cos \theta^*$	$d\sigma/d\Omega^*$ (mb/sr)	
	$\pi^+ - p$	$\pi^- - p$
1.000	6.520 ± 0.650	2.540 ± 0.250
0.628	4.386 ± 0.092	1.594 ± 0.041
0.558	3.552 ± 0.094	1.494 ± 0.046
0.480	3.090 ± 0.126	1.412 ± 0.078
0.392	2.483 ± 0.150	1.190 ± 0.088
0.292	1.844 ± 0.201	0.980 ± 0.107
0.191	1.070 ± 0.306	0.566 ± 0.139
0.091	1.116 ± 0.243	0.670 ± 0.102
-0.025	0.634 ± 0.040	0.426 ± 0.026
-0.136	0.351 ± 0.032	0.380 ± 0.022
-0.241	0.201 ± 0.027	0.276 ± 0.021
-0.370	0.104 ± 0.019	0.255 ± 0.015
-0.525	0.186 ± 0.019	0.355 ± 0.018
-0.655	0.268 ± 0.025	0.496 ± 0.023
-0.752	0.357 ± 0.032	0.717 ± 0.030
-0.824	0.534 ± 0.040	0.917 ± 0.039
-0.877	0.602 ± 0.046	1.077 ± 0.047
-0.945	0.599 ± 0.059	1.197 ± 0.059
-0.953	0.689 ± 0.051	1.161 ± 0.053

Table V. Differential cross-section data for $T_{\pi} = 490$ MeV.

$\text{Cos } \theta^*$	$d\sigma/d\Omega^*$ (mb/sr)	
	$\pi^+ - p$	$\pi^- - p$
1.000	5.170 ± 0.520	3.570 ± 0.360
0.685	3.701 ± 0.091	1.866 ± 0.057
0.617	3.751 ± 0.079	1.879 ± 0.046
0.545	2.960 ± 0.080	1.558 ± 0.051
0.466	2.471 ± 0.112	1.433 ± 0.089
0.376	2.140 ± 0.131	1.286 ± 0.097
0.276	1.279 ± 0.179	0.941 ± 0.118
0.173	0.819 ± 0.220	0.620 ± 0.127
0.073	0.645 ± 0.310	0.494 ± 0.165
-0.043	0.419 ± 0.042	0.498 ± 0.030
-0.154	0.243 ± 0.028	0.288 ± 0.023
-0.258	0.093 ± 0.024	0.255 ± 0.020
-0.386	0.061 ± 0.016	0.235 ± 0.015
-0.538	0.100 ± 0.019	0.321 ± 0.018
-0.665	0.169 ± 0.021	0.589 ± 0.026
-0.760	0.241 ± 0.028	0.781 ± 0.034
-0.830	0.342 ± 0.031	1.009 ± 0.043
-0.881	0.402 ± 0.038	1.101 ± 0.057
-0.918	0.378 ± 0.047	1.292 ± 0.064
-0.954	0.353 ± 0.041	1.513 ± 0.058

Table VI. Differential cross-section data for $T_{\pi} = 550$ MeV.

$\text{Cos } \theta^*$	$d\sigma/d\Omega^*$ (mb/sr)	
	$\pi^+ - p$	$\pi^- - p$
1.000	3.850 ± 0.380	5.410 ± 0.540
0.728	3.046 ± 0.068	2.951 ± 0.075
0.671	2.792 ± 0.065	2.702 ± 0.071
0.600	2.661 ± 0.055	2.422 ± 0.057
0.526	2.192 ± 0.060	2.061 ± 0.063
0.445	1.771 ± 0.078	1.634 ± 0.082
0.354	1.403 ± 0.085	1.419 ± 0.095
0.251	0.923 ± 0.121	1.014 ± 0.124
0.148	0.523 ± 0.184	0.567 ± 0.175
0.047	0.418 ± 0.194	0.413 ± 0.183
-0.070	0.299 ± 0.026	0.189 ± 0.031
-0.180	0.154 ± 0.020	0.161 ± 0.023
-0.283	0.067 ± 0.018	0.133 ± 0.022
-0.408	0.053 ± 0.014	0.190 ± 0.016
-0.556	0.104 ± 0.014	0.406 ± 0.022
-0.679	0.138 ± 0.016	0.724 ± 0.031
-0.771	0.152 ± 0.020	1.031 ± 0.040
-0.838	0.155 ± 0.023	1.219 ± 0.056
-0.887	0.146 ± 0.027	1.394 ± 0.065
-0.922	0.125 ± 0.032	1.832 ± 0.084
-0.957	0.133 ± 0.026	1.696 ± 0.075

Table VII. Differential cross-section data for $T_{\pi} = 600$ MeV.

$\text{Cos}\theta^*$	$d\sigma/d\Omega^*$ (mb/sr)	
	$\pi^+ - p$	$\pi^- - p$
1.000	2.890 ± 0.290	6.930 ± 0.690
0.718	2.340 ± 0.055	3.778 ± 0.088
0.659	2.118 ± 0.052	3.289 ± 0.082
0.586	1.994 ± 0.044	2.995 ± 0.069
0.511	1.576 ± 0.050	2.462 ± 0.075
0.428	1.406 ± 0.068	1.888 ± 0.087
0.335	1.041 ± 0.071	1.449 ± 0.097
0.231	0.669 ± 0.097	1.037 ± 0.133
0.127	0.419 ± 0.167	0.569 ± 0.238
0.026	0.384 ± 0.105	0.356 ± 0.156
-0.090	0.200 ± 0.022	0.207 ± 0.029
-0.200	0.108 ± 0.019	0.081 ± 0.023
-0.302	0.068 ± 0.019	0.103 ± 0.024
-0.425	0.043 ± 0.016	0.185 ± 0.022
-0.570	0.091 ± 0.016	0.449 ± 0.026
-0.691	0.182 ± 0.018	0.640 ± 0.034
-0.779	0.151 ± 0.020	0.950 ± 0.045
-0.844	0.135 ± 0.022	1.028 ± 0.053
-0.891	0.107 ± 0.024	1.155 ± 0.064
-0.925	0.126 ± 0.027	1.216 ± 0.079
-0.958	0.082 ± 0.027	1.340 ± 0.072

Table VIII. Differential cross-section data for $T_{\pi} = 650$ MeV.

$\text{Cos } \theta^*$	$d\sigma/d\Omega^*$ (mb/sr)	
	$\pi^+ - p$	$\pi^- - p$
1.000	2.340 ± 0.230	6.430 ± 0.640
0.708	1.786 ± 0.046	3.170 ± 0.085
0.648	1.599 ± 0.047	2.756 ± 0.081
0.573	1.590 ± 0.039	2.379 ± 0.064
0.496	1.301 ± 0.048	1.951 ± 0.077
0.412	1.048 ± 0.058	1.444 ± 0.086
0.317	0.795 ± 0.064	1.228 ± 0.096
0.212	0.496 ± 0.087	0.833 ± 0.125
0.107	0.240 ± 0.104	0.252 ± 0.155
0.006	0.168 ± 0.143	0.155 ± 0.226
-0.110	0.111 ± 0.023	0.171 ± 0.033
-0.219	0.009 ± 0.019	0.153 ± 0.025
-0.320	0.072 ± 0.018	0.204 ± 0.027
-0.441	0.128 ± 0.016	0.343 ± 0.024
-0.584	0.158 ± 0.018	0.618 ± 0.032
-0.701	0.171 ± 0.020	0.676 ± 0.039
-0.787	0.233 ± 0.021	0.820 ± 0.045
-0.850	0.207 ± 0.023	0.797 ± 0.050
-0.895	0.151 ± 0.028	0.650 ± 0.059
-0.928	0.121 ± 0.029	0.763 ± 0.064
-0.960	0.125 ± 0.027	0.755 ± 0.058

Table IX. Coefficients of powers of $\cos \theta^*$ (π^+ -p).

a	Pion kinetic energy in lab system (MeV)							
	310	370	410	450	490	550	600	650
a_0	1.958±0.051	1.256±0.031	0.905±0.036	0.691±0.026	0.554±0.034	0.412±0.017	0.312±0.015	0.207±0.022
a_1	4.697±0.253	3.968±0.140	3.558±0.167	3.038±0.118	2.692±0.138	1.988±0.068	1.546±0.060	1.192±0.070
a_2	8.925±0.472	5.670±0.209	5.112±0.218	4.260±0.147	3.771±0.171	2.960±0.088	2.446±0.087	2.348±0.118
a_3	0.297±0.644	0.193±0.416	0.249±0.458	0.305±0.329	-0.022±0.353	0.053±0.162	0.044±0.144	-0.102±0.168
a_4	-0.719±0.754	-0.314±0.440	-0.871±0.485	-0.880±0.334	-1.280±0.362	-1.272±0.171	-1.234±0.158	-1.440±0.194

a. Coefficients

Table X. Coefficients of powers of $\cos\theta^*$ (π^- -p).

Coefficients	Pion kinetic energy in lab system (MeV)						
	370	410	450	490	550	600	650
a_0	0.561±0.014	0.537±0.013	0.497±0.021	0.518±0.029	0.347±0.029	0.343±0.024	0.274±0.034
a_1	0.964±0.045	1.092±0.045	1.316±0.092	1.501±0.115	1.718±0.112	2.039±0.094	1.371±0.121
a_2	1.076±0.098	1.285±0.085	1.371±0.139	1.347±0.194	3.095±0.218	4.081±0.193	3.914±0.263
a_3	-0.858±0.089	-0.786±0.104	-1.220±0.377	-1.425±0.469	-0.501±0.485	-0.041±0.405	0.332±0.523
a_4	-0.449±0.126	-0.290±0.134	0.080±0.233	0.621±0.352	0.138±0.390	-0.608±0.360	-1.057±0.469
a_5	--	--	0.460±0.361	0.773±0.495	0.117±0.558	0.439±0.482	0.847±0.609

Table XI. Order of fit (N), degrees of freedom (d), and goodness-of-fit $(\chi^2/d)^{1/2}$ parameter at each energy ($\pi^+ - p$).

<u>Energy</u>	<u>N</u>	<u>d</u>	<u>$(\chi^2/d)^{1/2}$</u>
310	4	12	0.788
370	4	13	0.793
410	4	14	1.174
450	4	14	1.051
490	4	15	1.442
550	4	16	1.032
600	4	16	1.077
650	4	16	1.438

Table XII. Order of fit (N), degrees of freedom (d), and goodness-of-fit $(\chi^2/d)^{1/2}$ parameter at each energy (π^- -p).

<u>Energy</u>	<u>N</u>	<u>d</u>	<u>$(\chi^2/d)^{1/2}$</u>
370	4	13	0.991
410	4	14	0.911
450	5	13	1.124
490	5	14	1.301
550	5	15	1.158
600	5	15	0.878
650	5	15	1.123

Table XIII. Total elastic cross sections from integration of differential cross sections.

Energy	$\sigma_{\text{tot el}} \text{ (mb)}$	
	$\pi^+ \text{-p}$	$\pi^- \text{-p}$
310	60.19 ± 1.41	--
370	38.74 ± 0.73	10.42 ± 0.17
410	30.59 ± 0.66	11.40 ± 0.16
450	24.31 ± 0.49	12.19 ± 0.26
490	19.55 ± 0.46	13.71 ± 0.35
550	14.38 ± 0.19	16.98 ± 0.37
600	11.06 ± 0.18	19.87 ± 0.34
650	8.82 ± 0.22	17.19 ± 0.45

Table XIV. Breit-Wigner parameters assumed for P_{33} , D_{13} ,
and F_{15} resonances.

State	E_R	$x = \Gamma_{el}/\Gamma$	Γ
P_{33}	4238	1.0	165
D_{13}	4512	0.8	110
F_{15}	4688	0.9	100

FIGURE CAPTIONS

- Fig. 1. Total cross sections for $\pi^\pm - p$, with lines indicating the energies at which the measurements of this experiment were made.
- Fig. 2. Plan view of the experimental arrangement. Symbols Q_1 , B_1 , B_2 , and Q_2 represent magnets. The beam counters are labeled M_1 , M_{1A} , M_2 , M_3 , and C. The counters, BeO target, and LH_2 target are not drawn to scale.
- Fig. 3. Plan view of array of scintillation counters.
- Fig. 4. Differential cross-section data and fitted curve for $\pi^+ - p$; $T_\pi = 310, 370, \text{ and } 440 \text{ MeV}$.
- Fig. 5. Differential cross-section data and fitted curve for $\pi^+ - p$; $T_\pi = 450, 490, 550, 600, \text{ and } 650 \text{ MeV}$.
- Fig. 6. Differential cross-section data and fitted curve for $\pi^- - p$; $T_\pi = 370, 410, 450, 490, \text{ and } 550 \text{ MeV}$.
- Fig. 7. Differential cross-section data and fitted curve for $\pi^- - p$; $T_\pi = 600 \text{ and } 650 \text{ MeV}$.
- Fig. 8. Coefficients of powers of $\cos \theta_\pi^*$ plotted vs pion energy ($\pi^+ - p$).
- Fig. 9. Coefficients of powers of $\cos \theta_\pi^*$ plotted vs pion energy ($\pi^- - p$). The dashed lines show the higher-energy behavior as indicated by the results of Helland et al. (reference 2a).
- Fig. 10. Total elastic cross sections plotted vs pion energy.
- Fig. 11. Circles showing the locus of Breit-Wigner scattering amplitudes for three values of the parameter x (where $x = \Gamma_{e1}/\Gamma$).
- Fig. 12. Assumed resonant behavior of the P_{33} , D_{13} , and F_{15} amplitudes.

- Fig. 13. Assumed behavior of the $S_{1/2}$, $P_{1/2}$, and D_{15} amplitudes.
- Fig. 14. Contribution to a_0 from $|D_{3/2}|^2$ and $S_{1/2}D_{3/2}$ terms.
- Fig. 15. Contribution to a_2 from $|D_{3/2}|^2$ and $S_{1/2}D_{3/2}$ terms.
- Fig. 16. Contribution to a_4 from $D_{3/2}D_{5/2}$ term.
- Fig. 17. Contribution to a_3 from $P_{3/2}D_{3/2}$ and $D_{5/2}F_{5/2}$ terms.
- Fig. 18. Contribution to a_1 from $P_{1/2}D_{3/2}$, $P_{3/2}D_{3/2}$, and $D_{5/2}F_{5/2}$ terms.
- Fig. 19. Energy dependence of π^- -p coefficients a_0 , a_1 , a_2 , and a_3 , a_4 , and a_5 , using the scattering amplitudes in Figs. 12 and 13. The data are plotted again for comparison. Δ , this experiment; O, Holland et al. (reference 2a).
- Fig. 20. Predicted recoil-proton polarization at 523, 572, and 689 MeV. The data are those of Eandi (reference 2d).

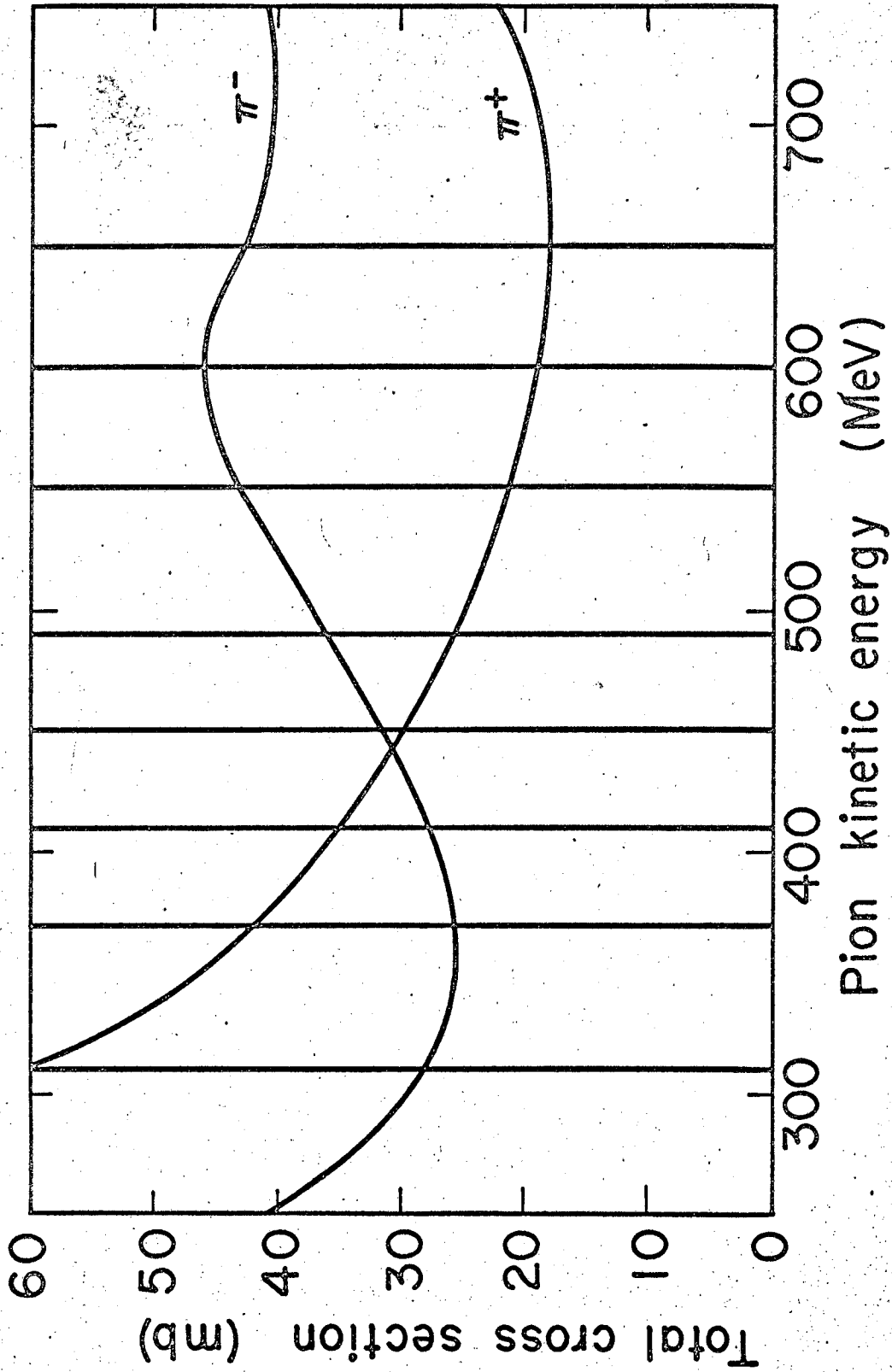


Fig. 1

MU-32811

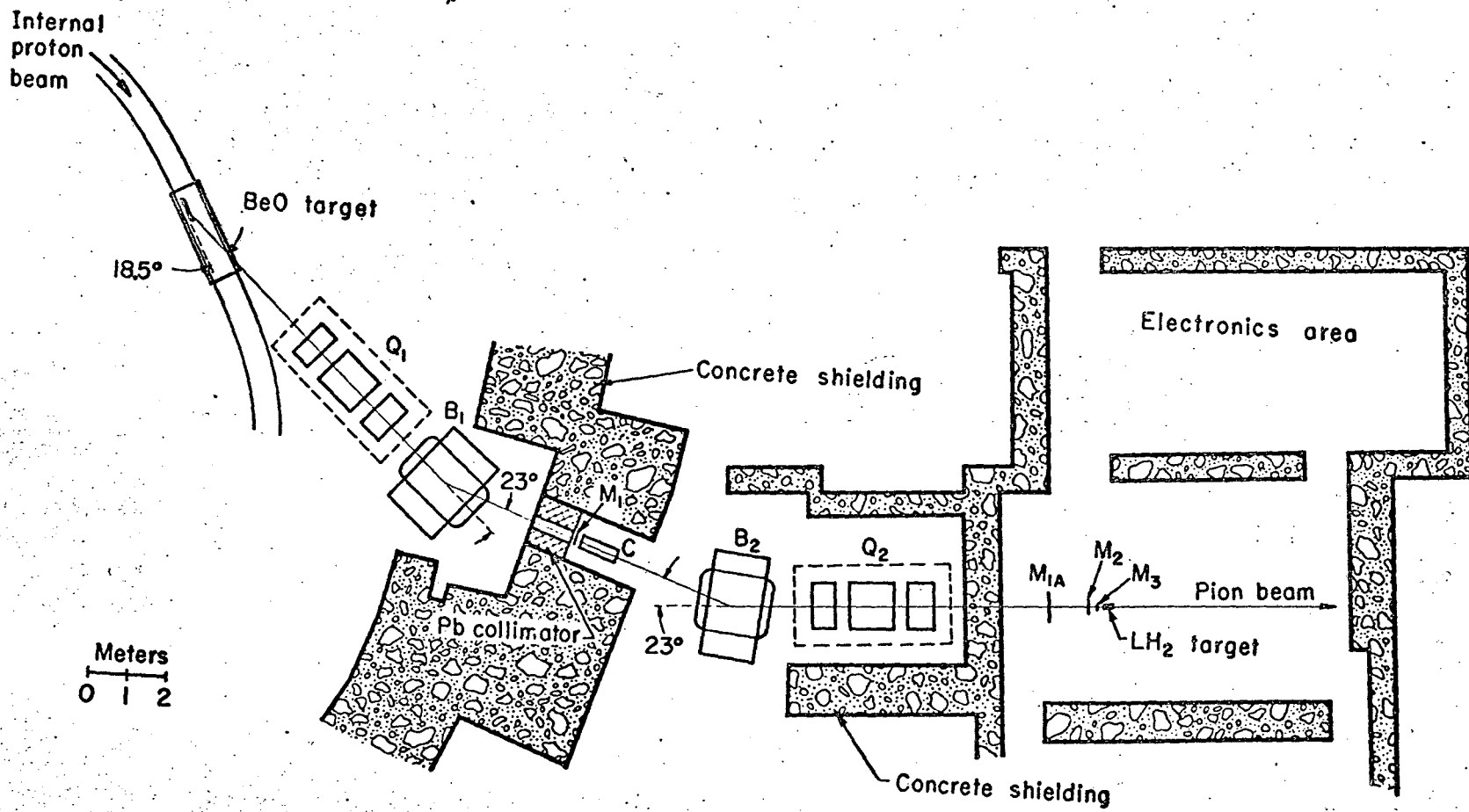
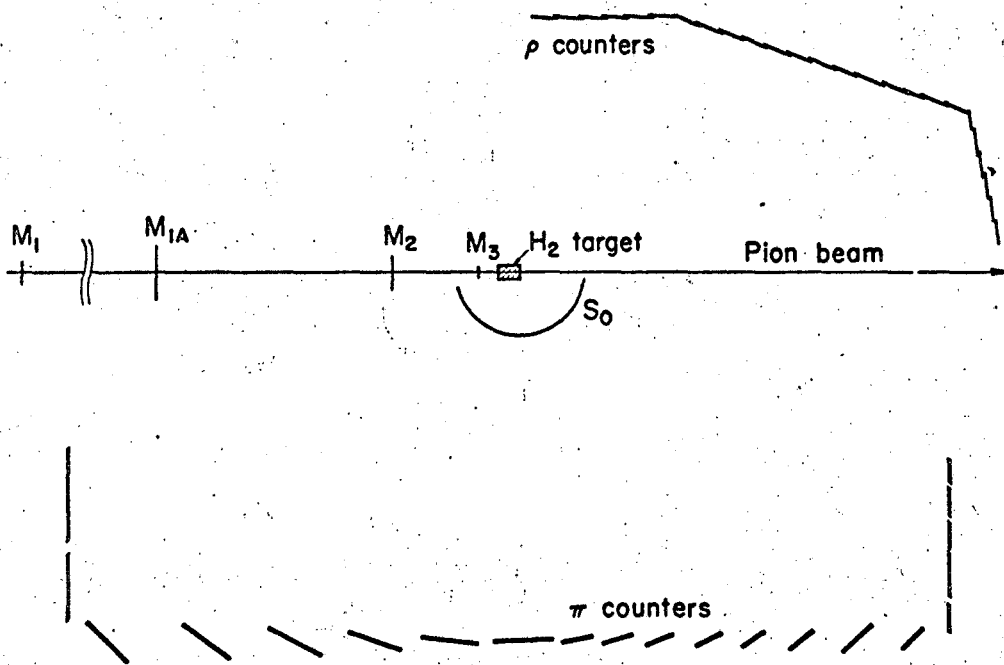


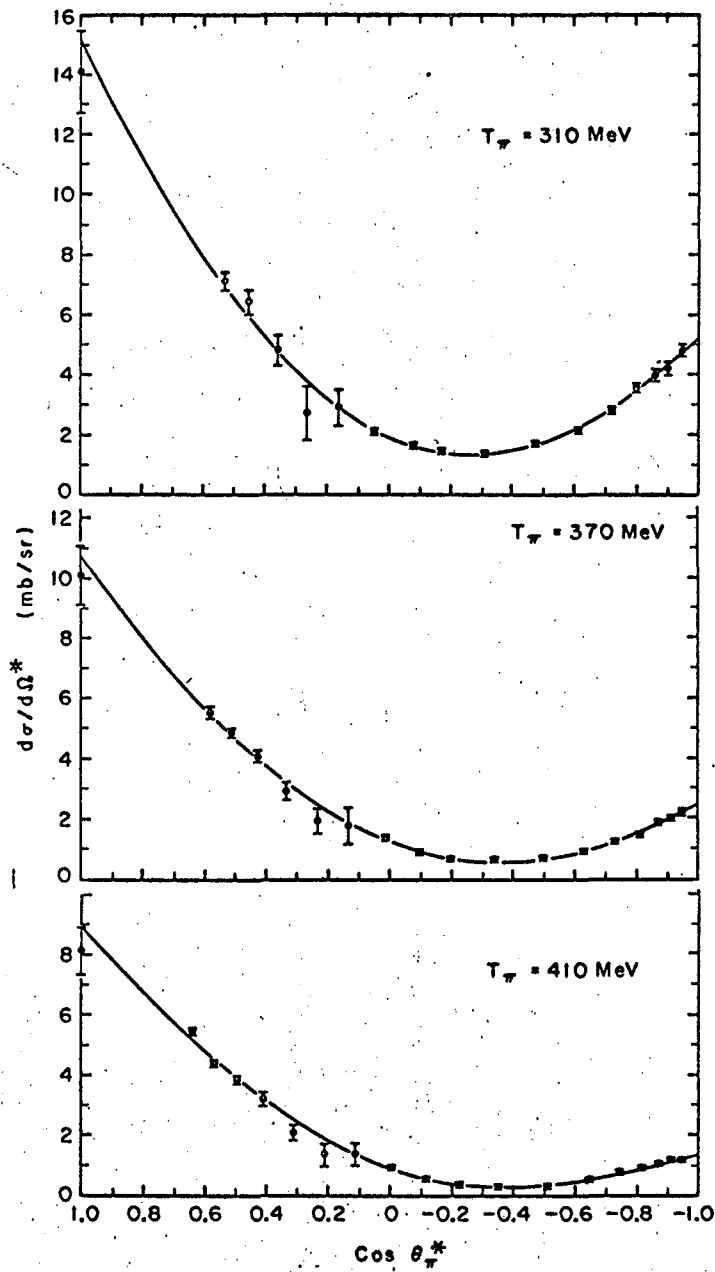
Fig. 2

MU-32812



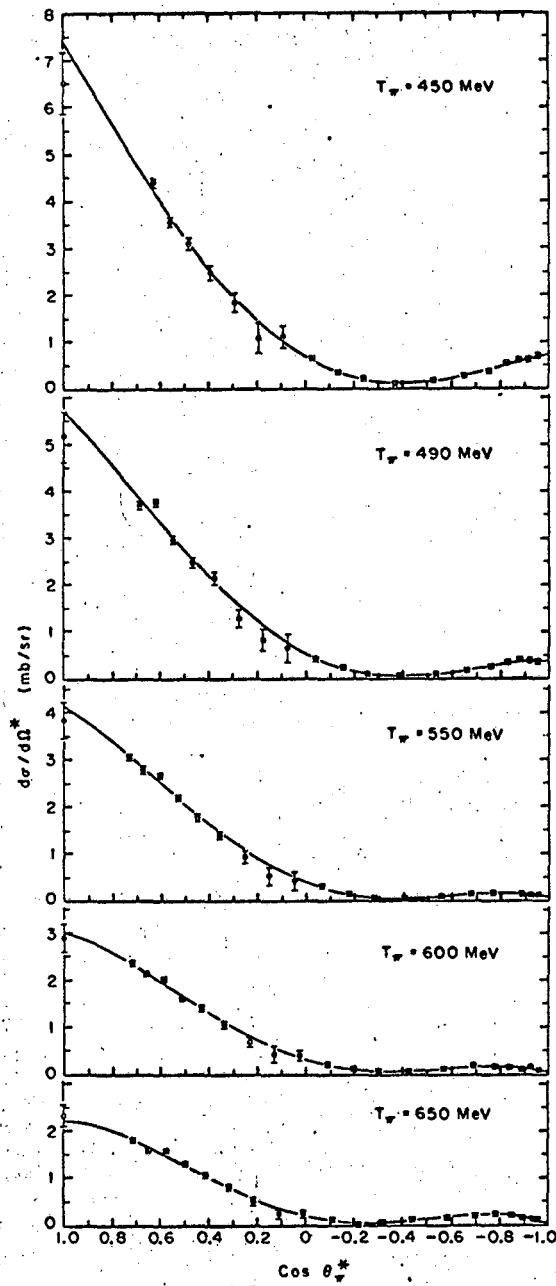
MUB-2350

Fig. 3



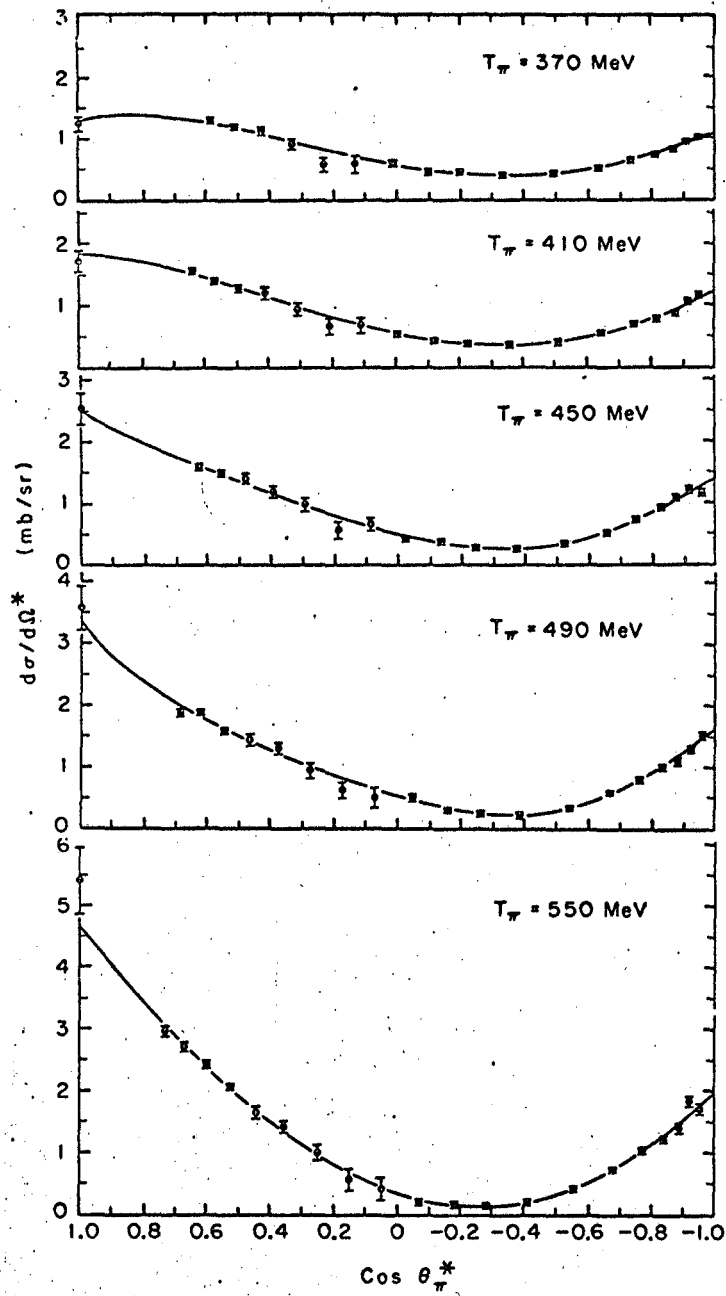
MUB-3956

Fig. 4



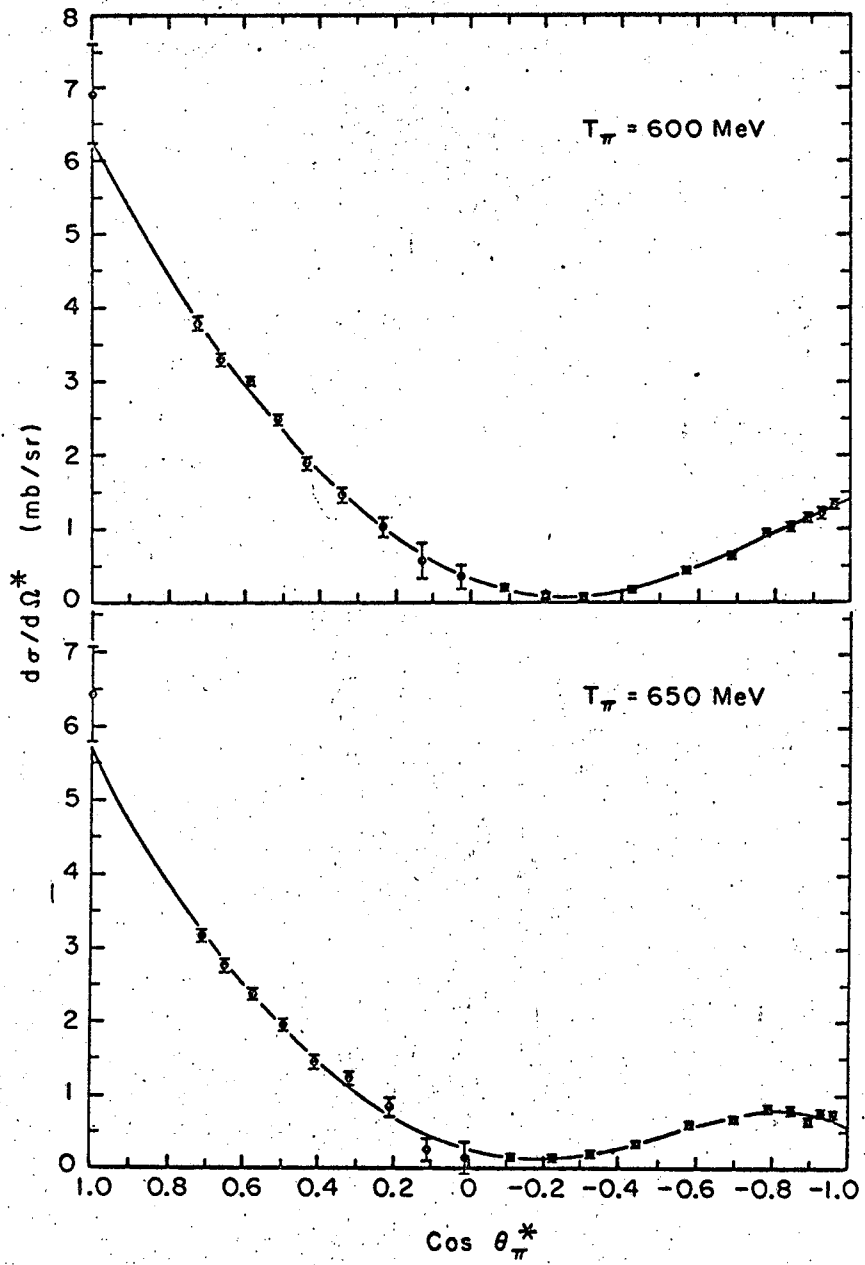
MUB-3957

Fig. 5



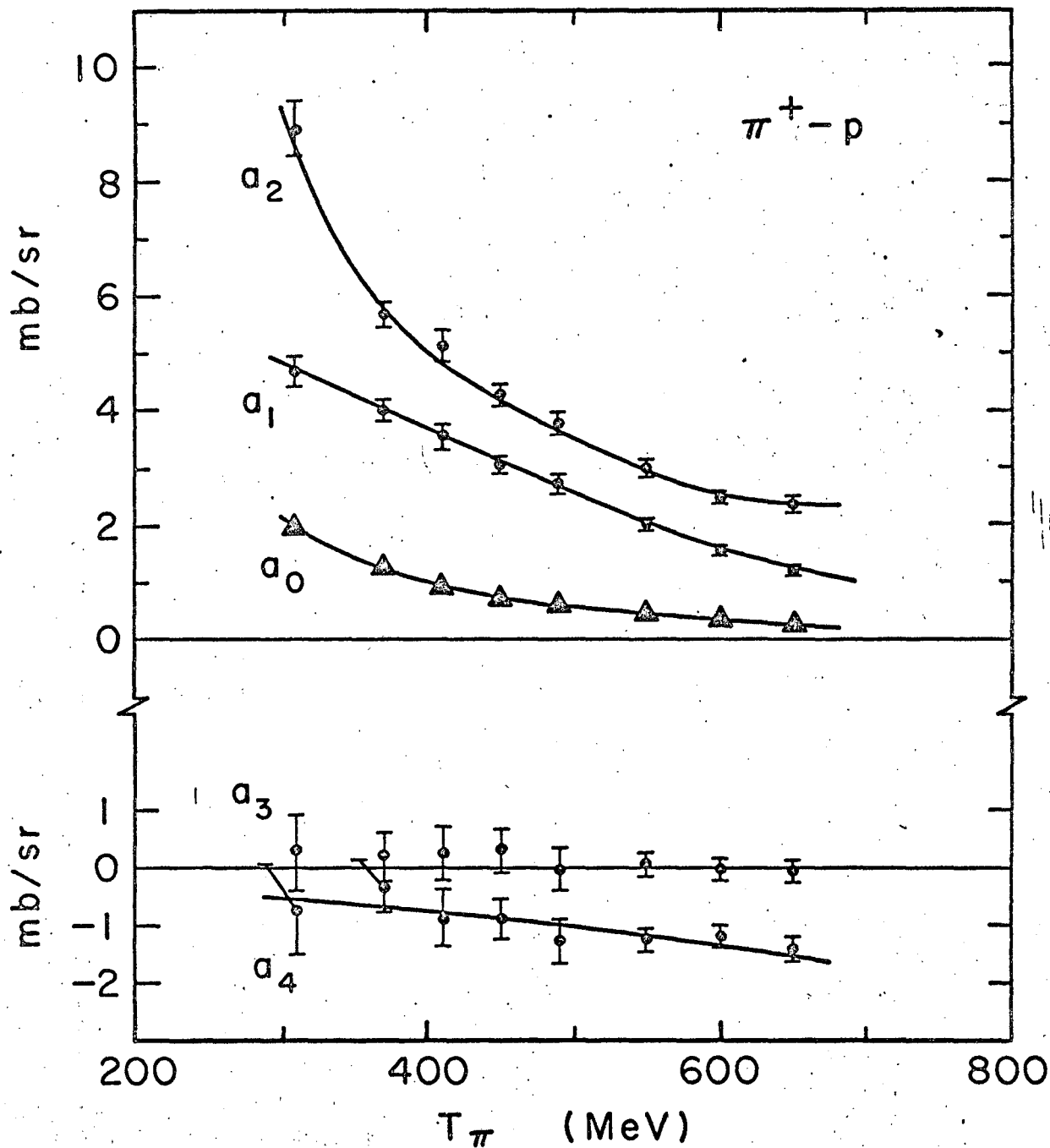
MUB-3958

Fig. 6



MUB-3959

Fig. 7



MU.33456

Fig. 8

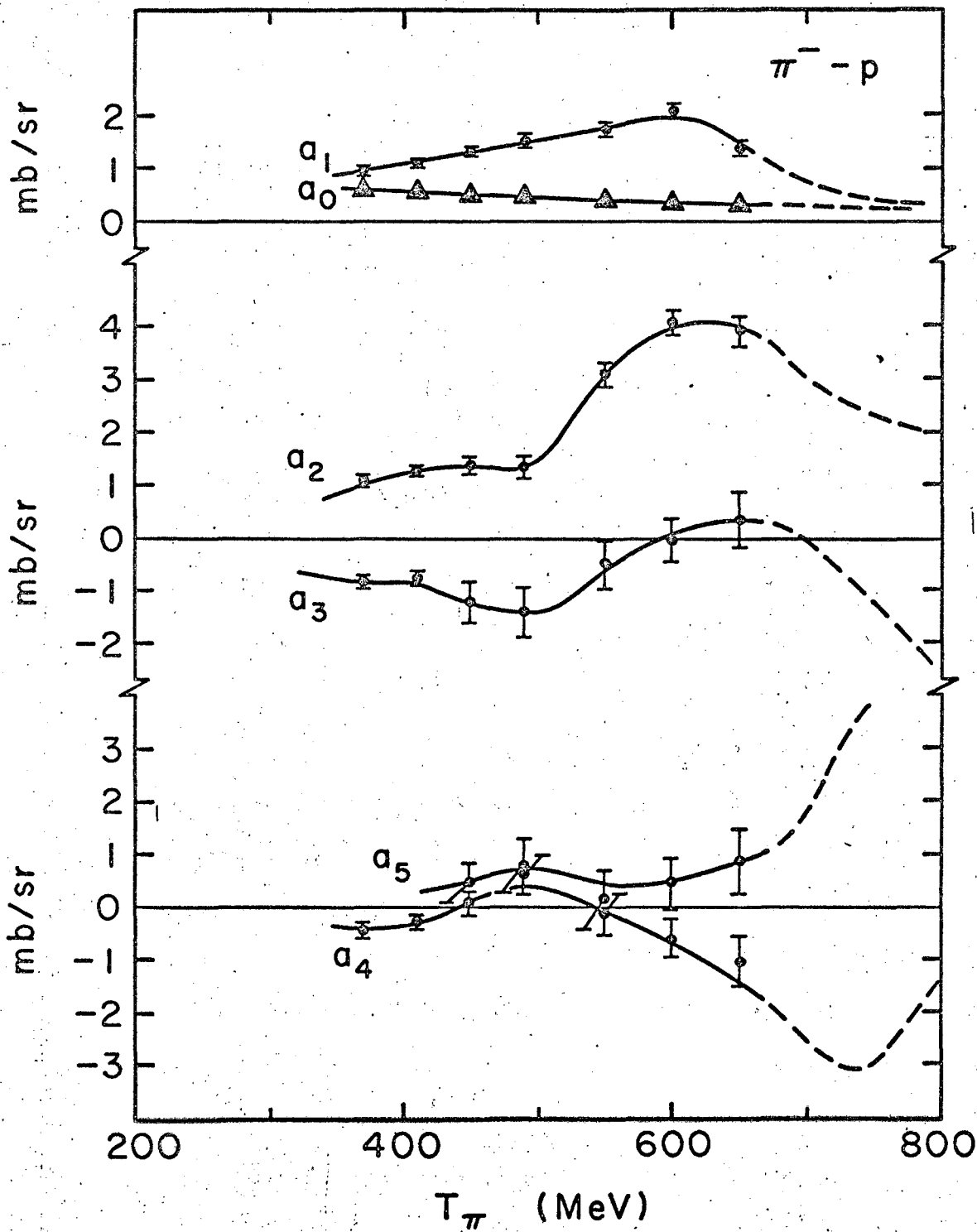
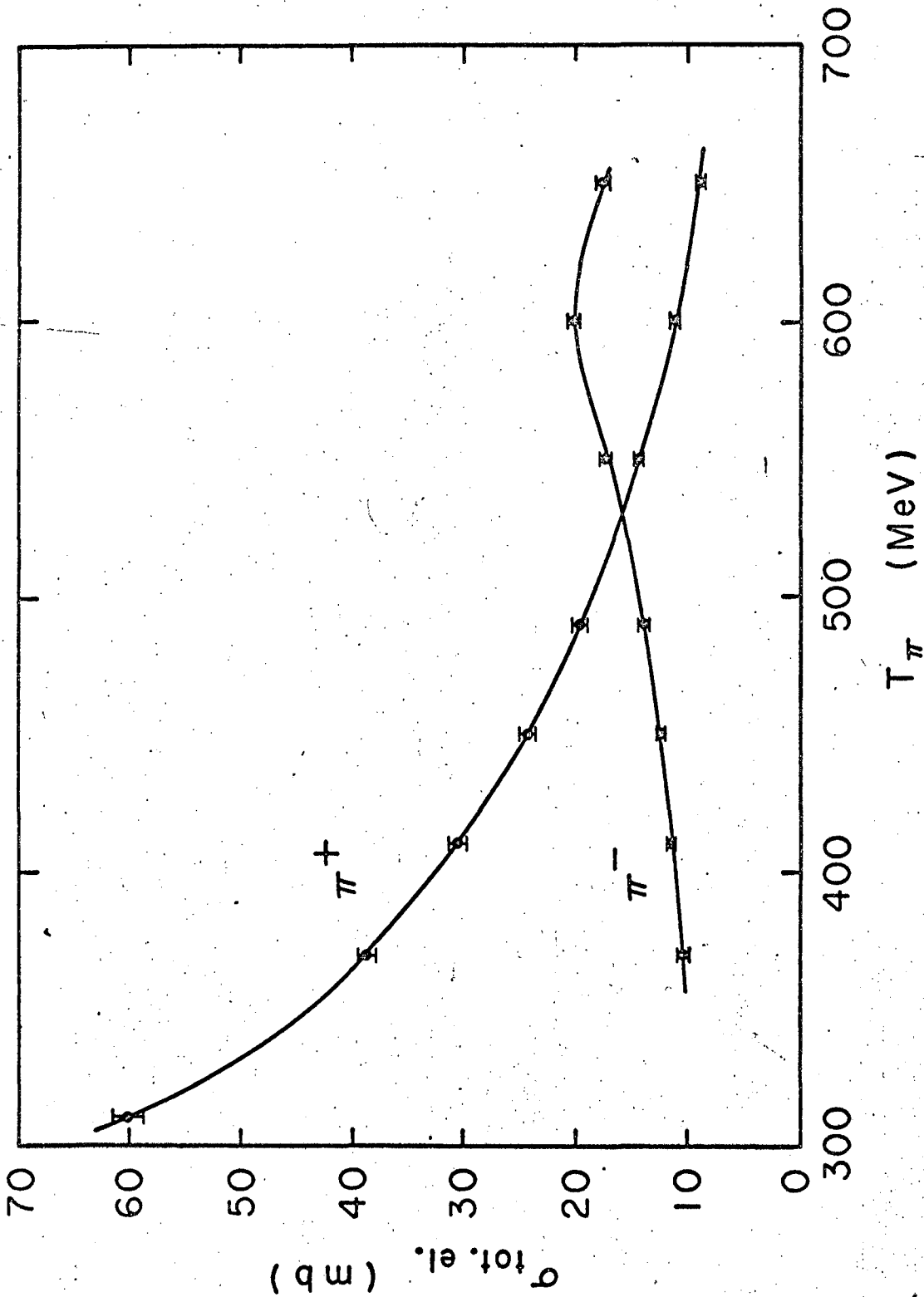


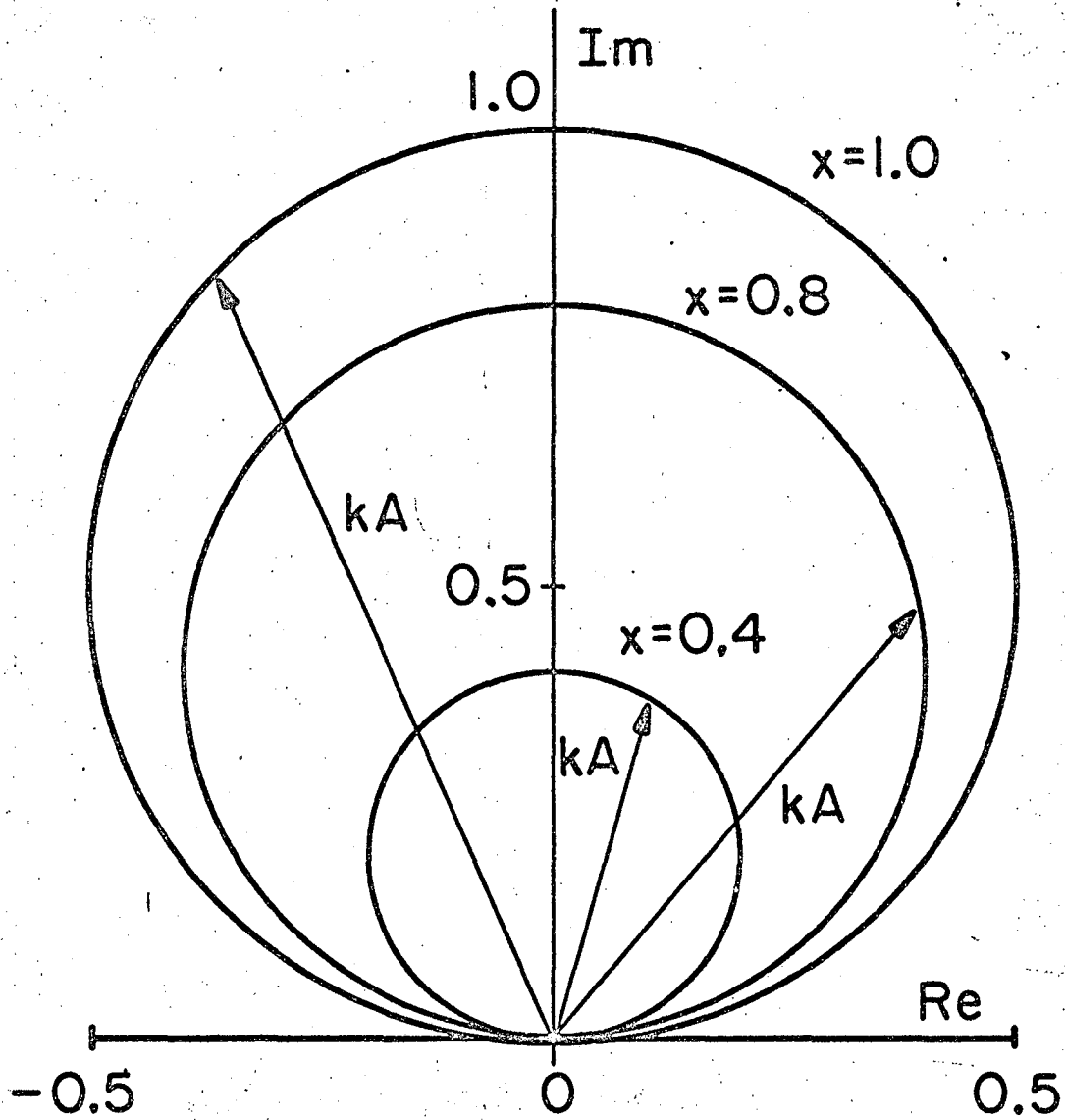
Fig. 9

MU-33457



MU-33458

Fig. 10



MU-33526

Fig. 11

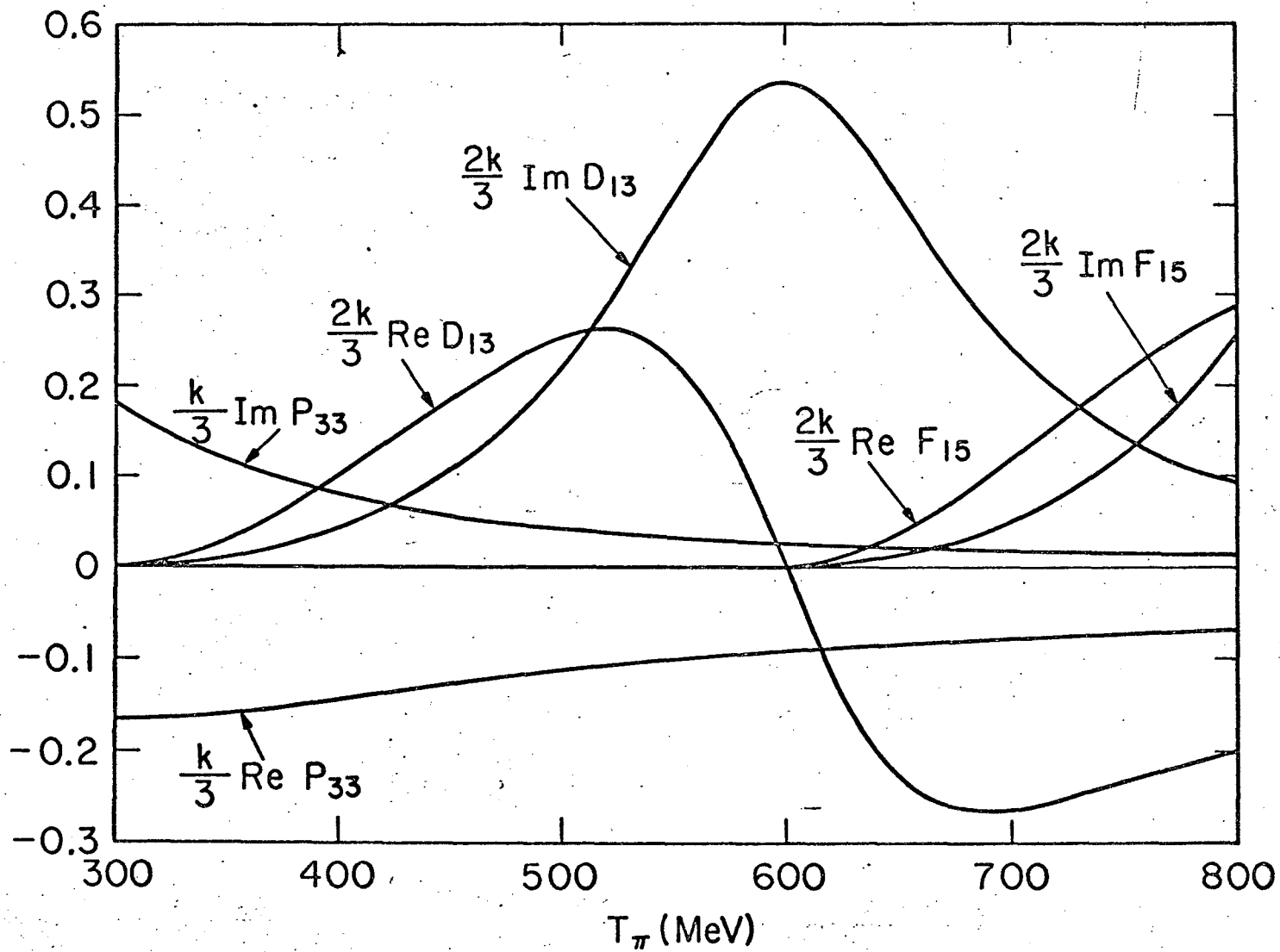


Fig. 12

MU-33527

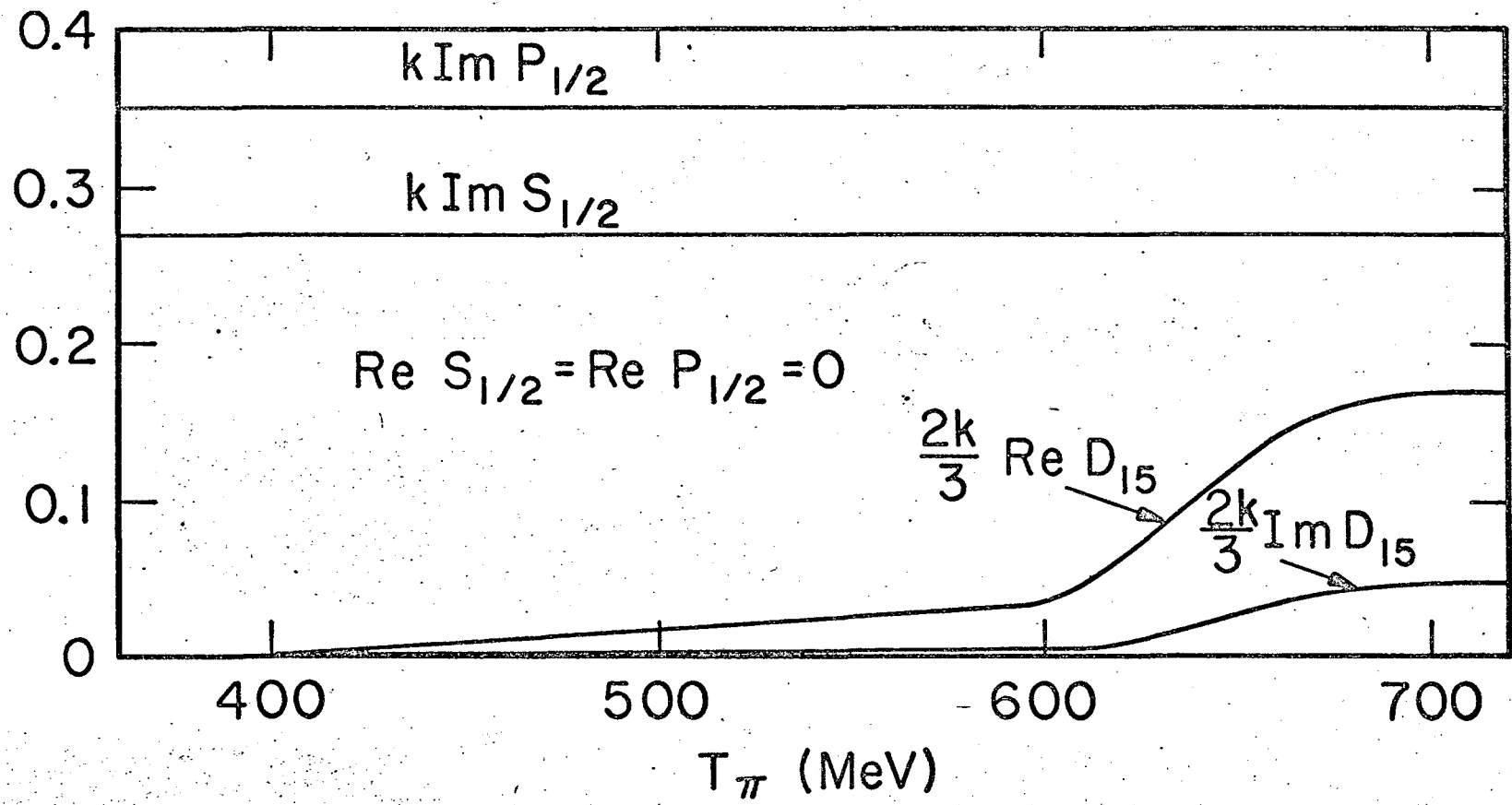
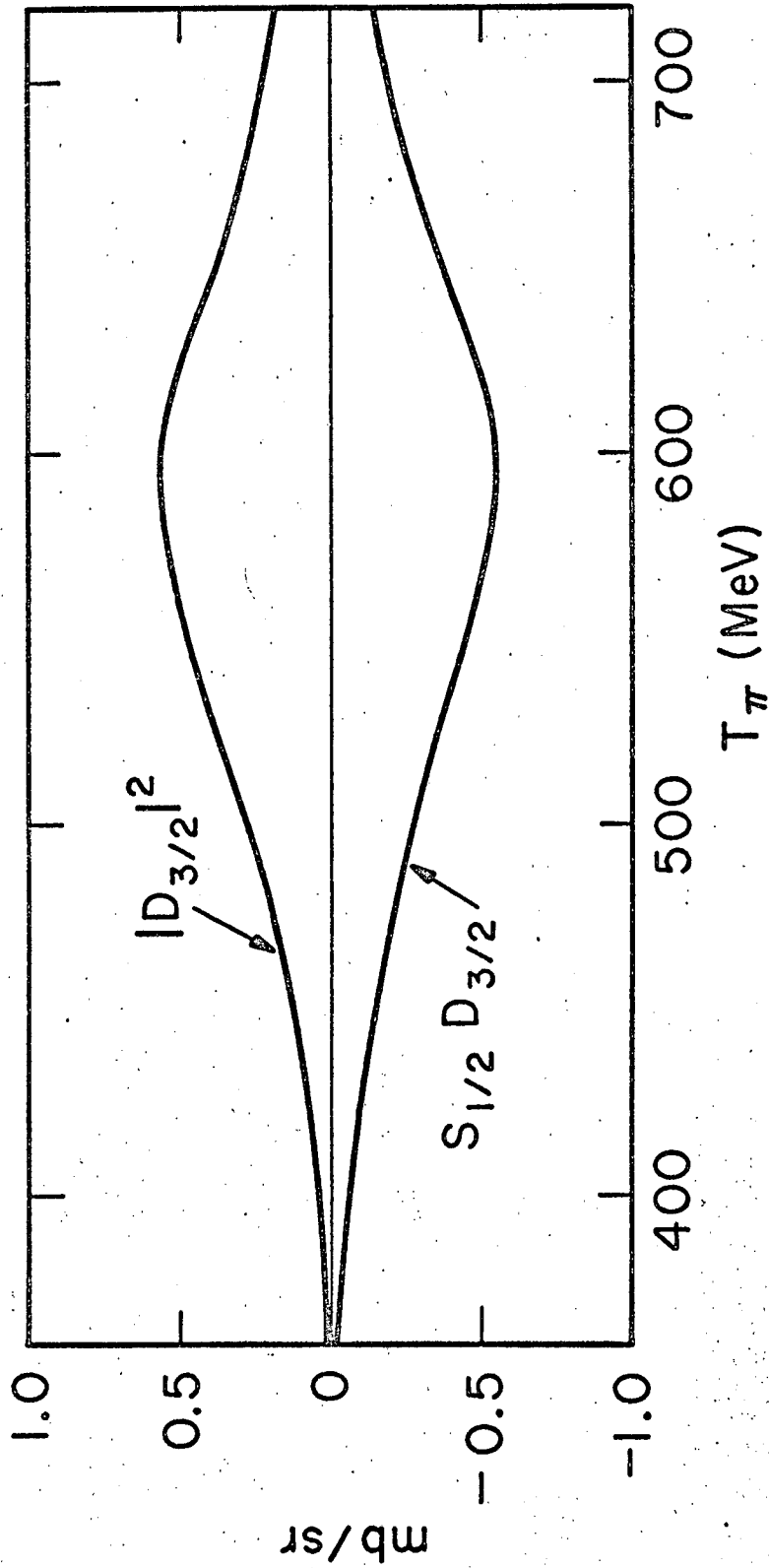


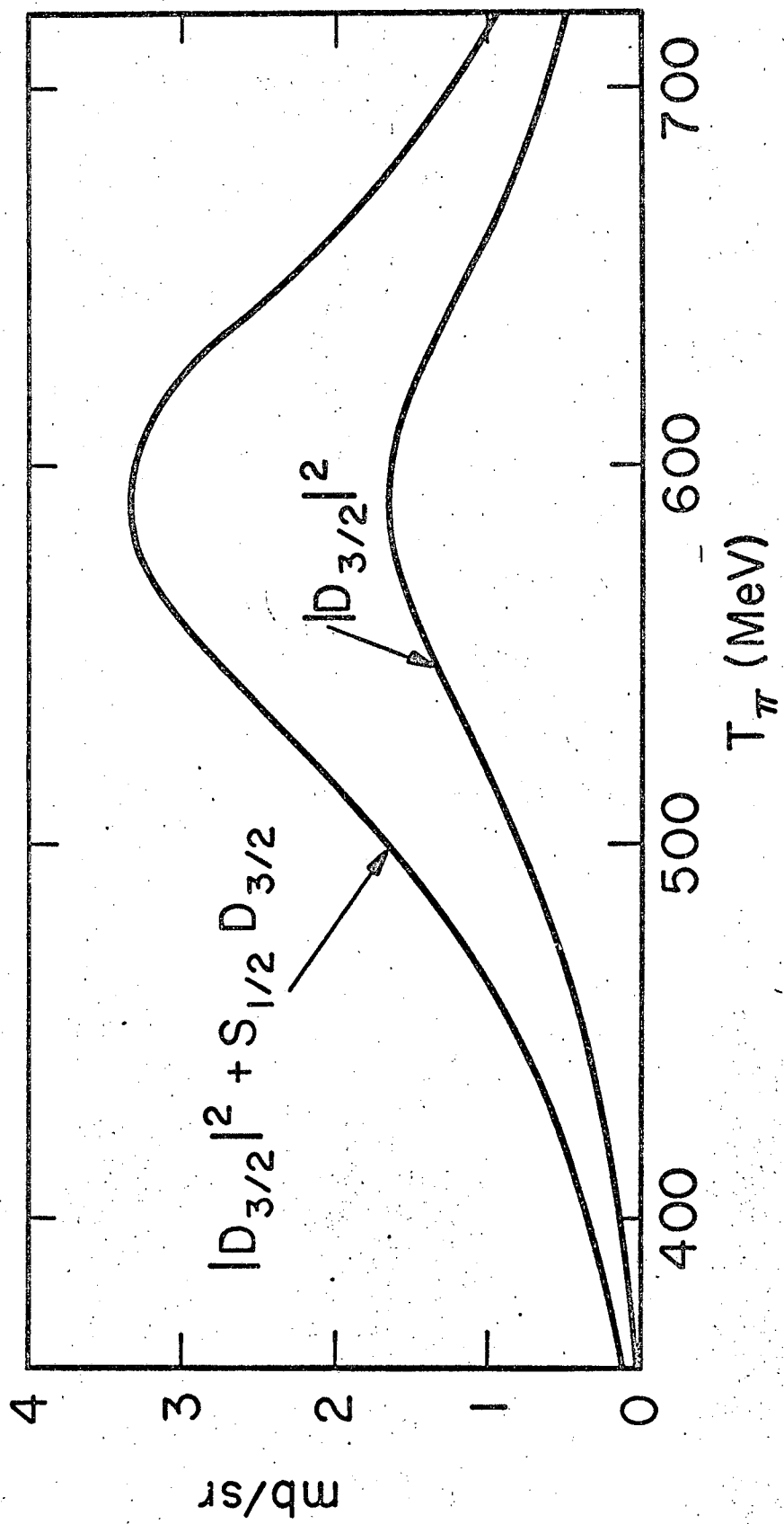
Fig. 13

MU-33528



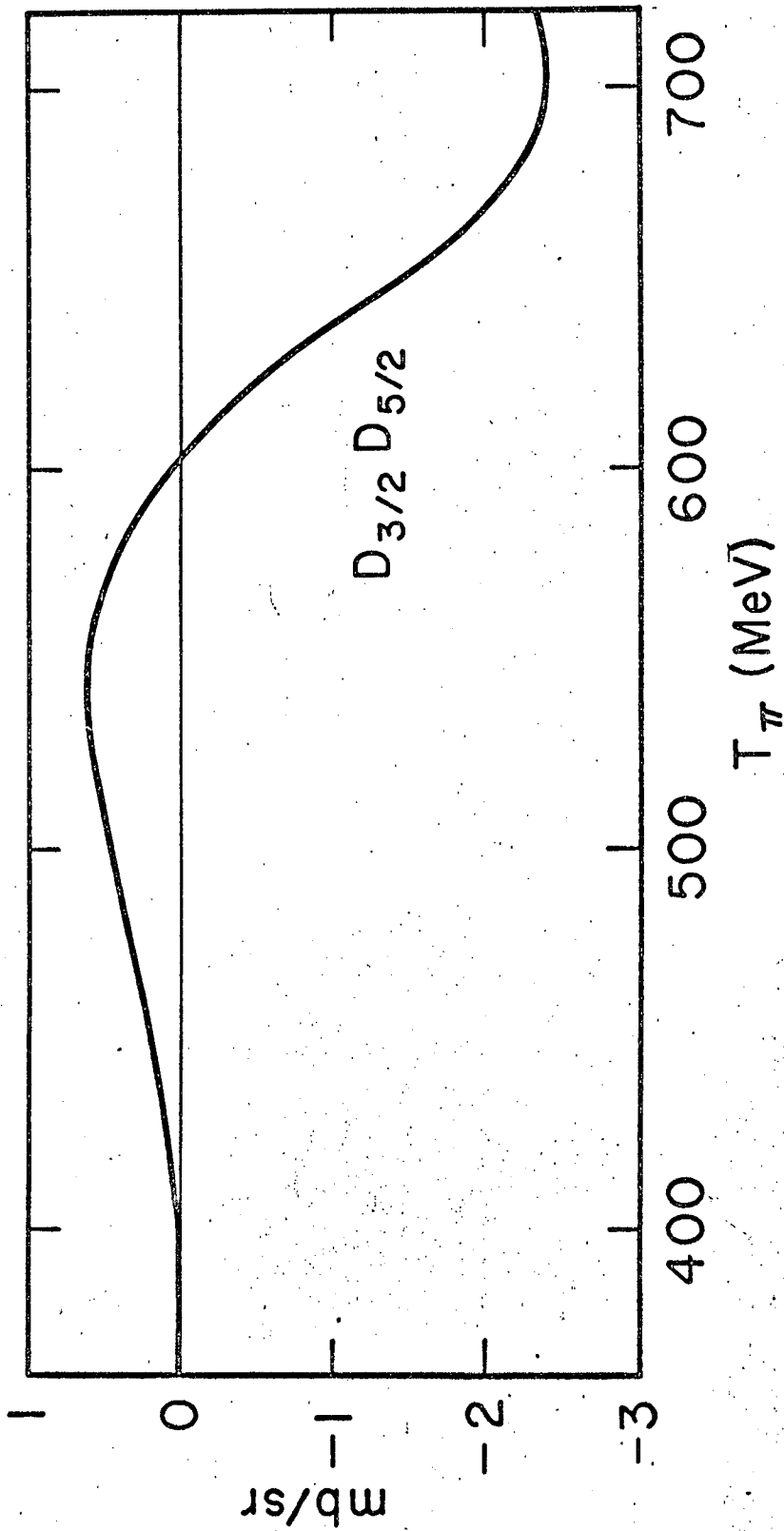
MU-33529

Fig. 14



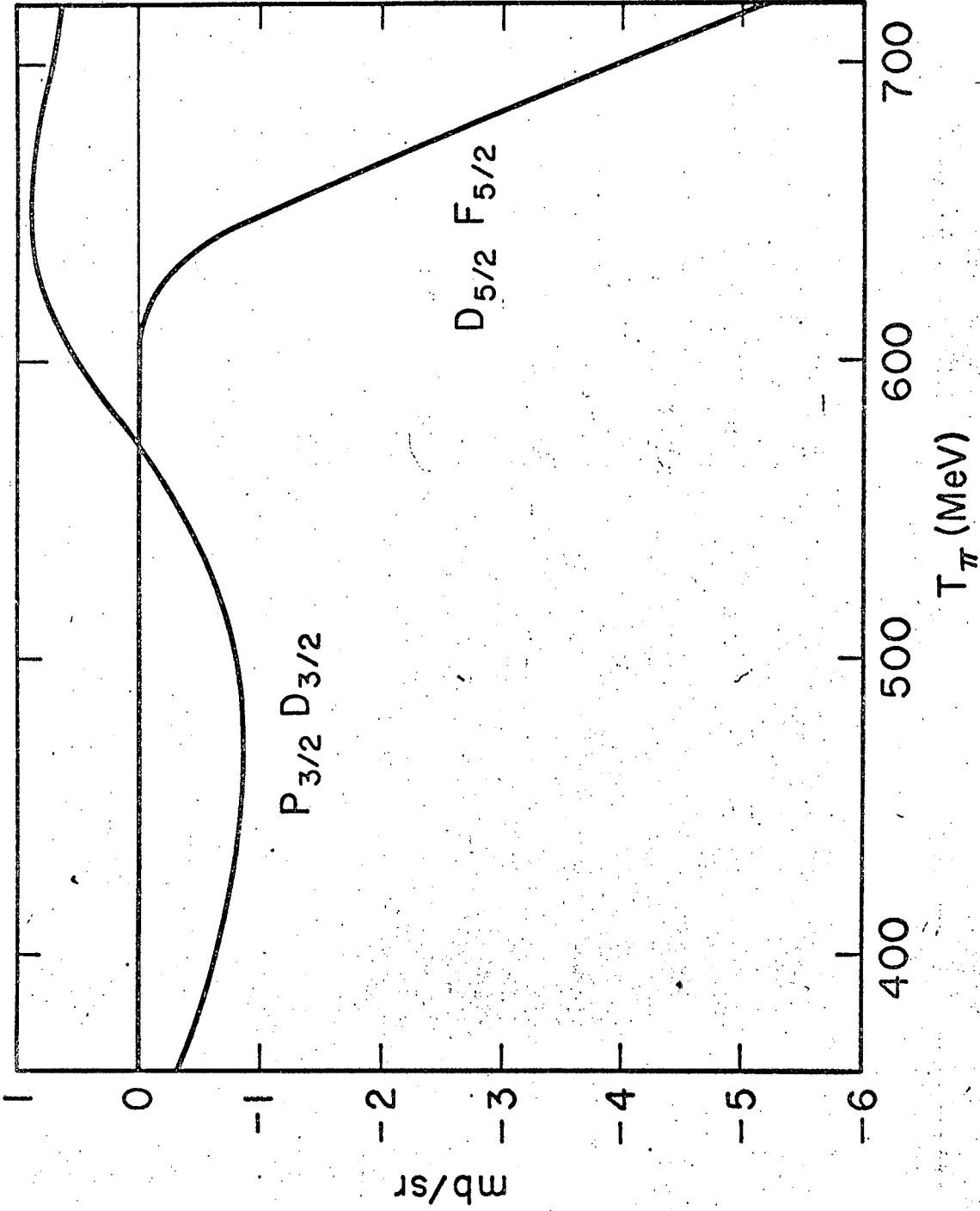
MU-33530

Fig. 15



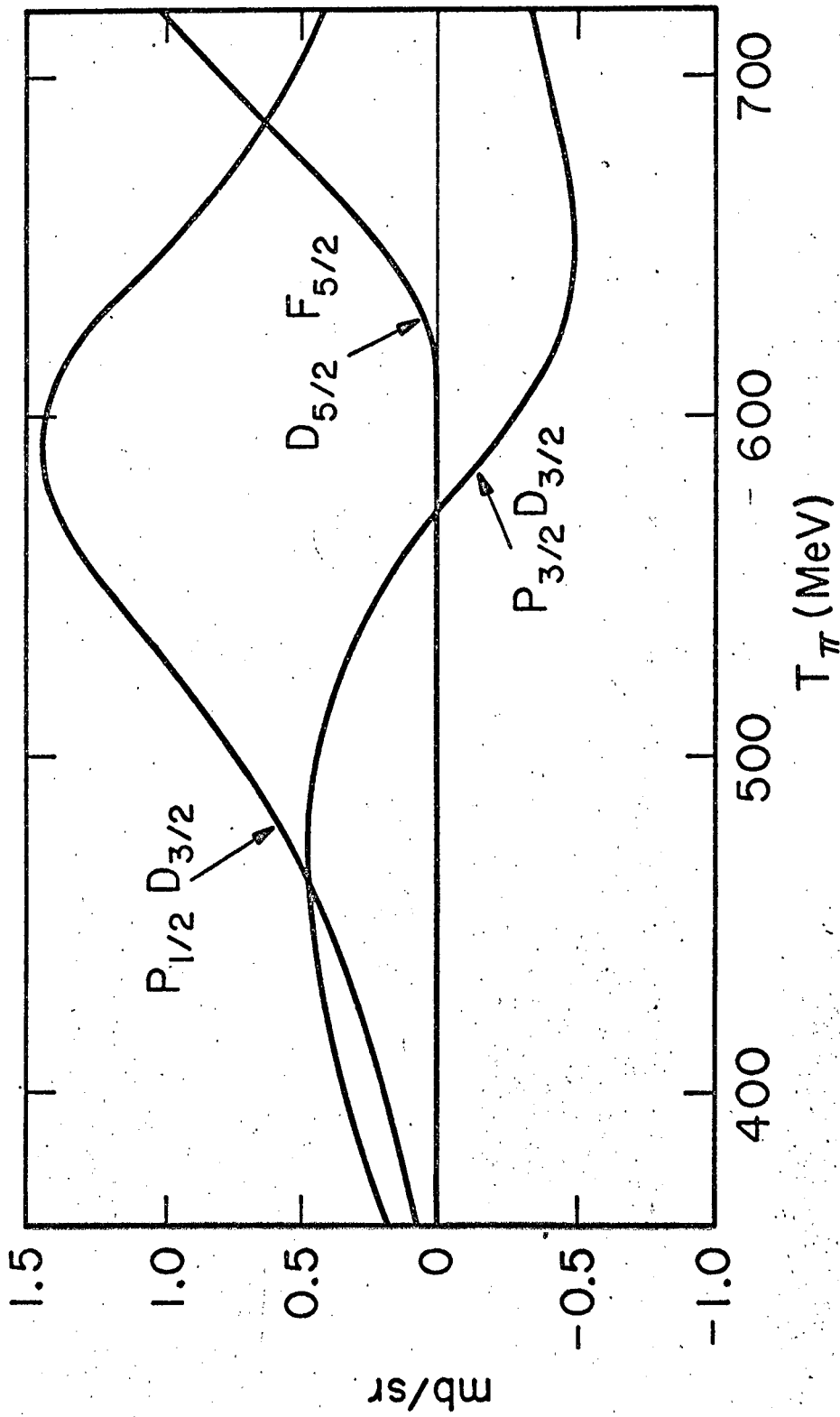
MU-33531

Fig. 16



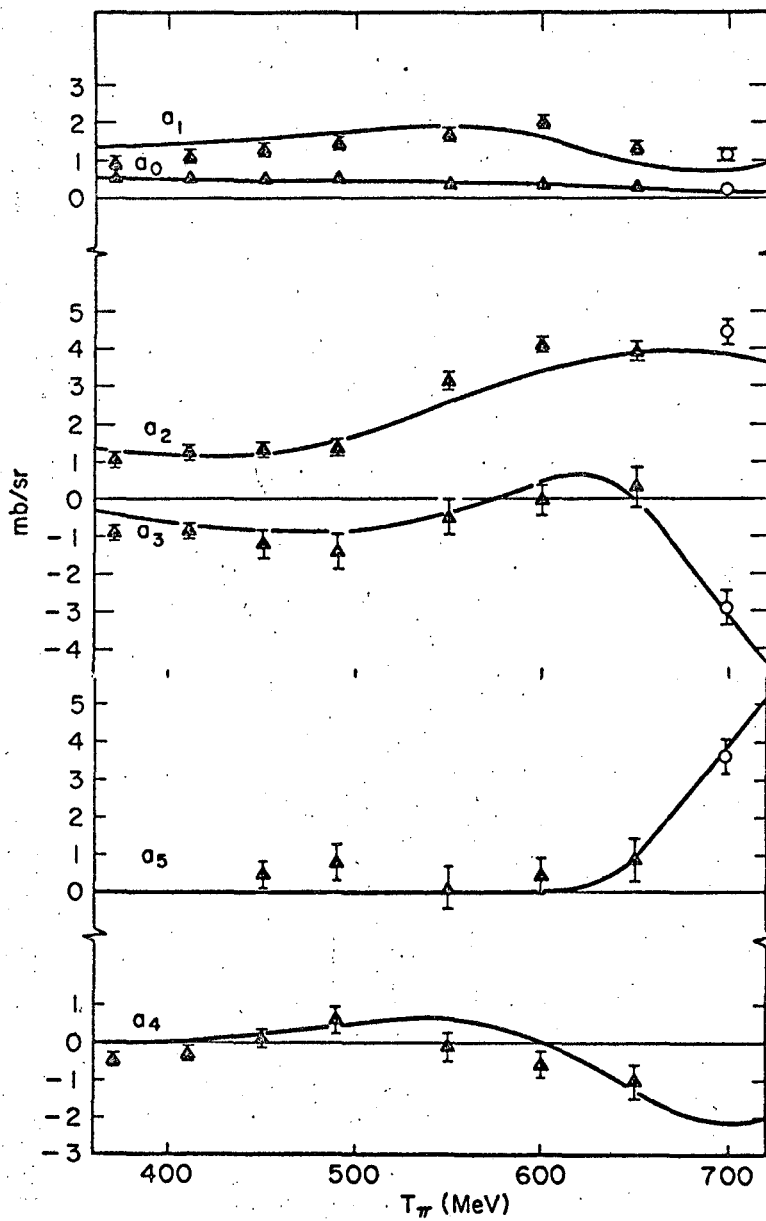
MU-33532

Fig. 17



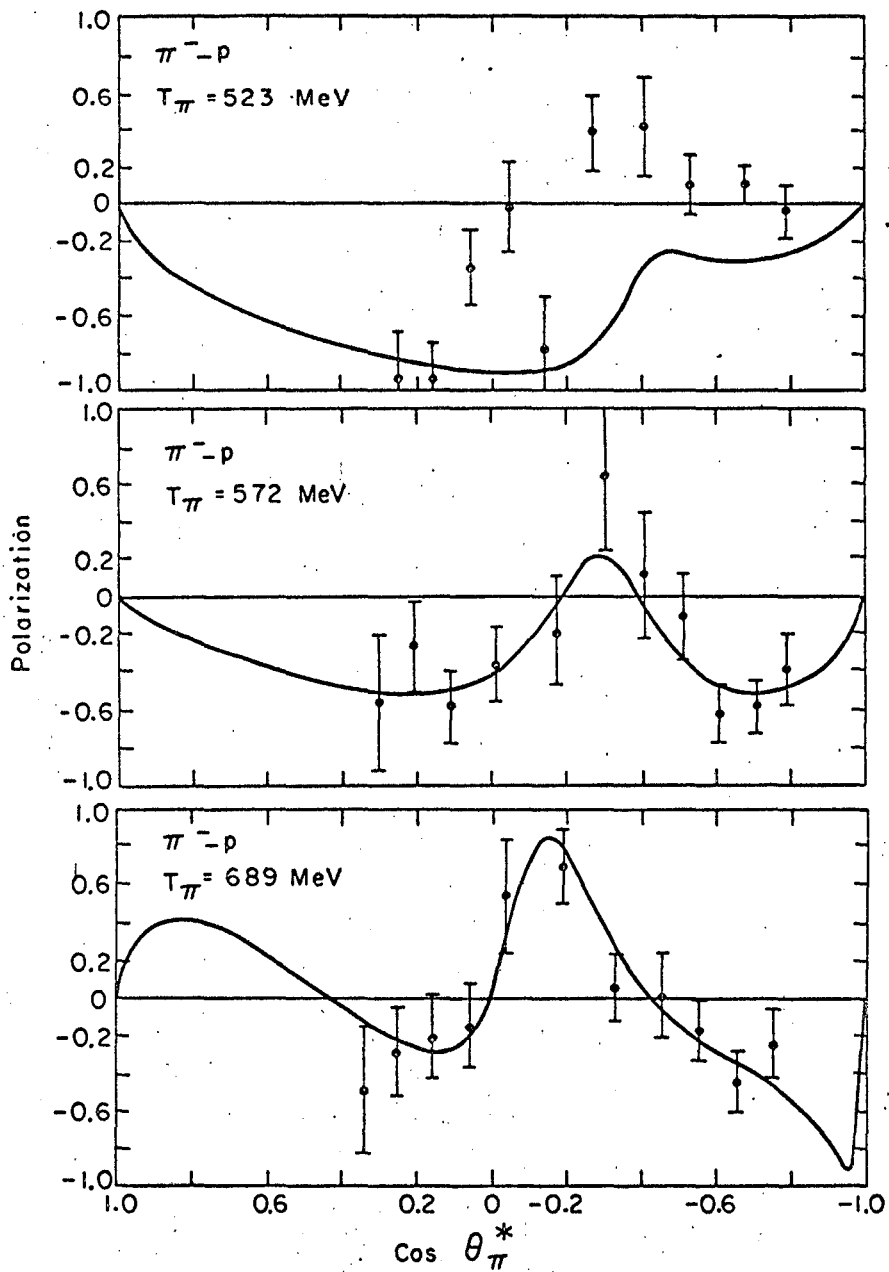
MU-33533

Fig. 18



MUB-3960

Fig. 19



MUB-3961

Fig. 20

This report was prepared as an account of Government sponsored work. Neither the United States, nor the Commission, nor any person acting on behalf of the Commission:

- A. Makes any warranty or representation, expressed or implied, with respect to the accuracy, completeness, or usefulness of the information contained in this report, or that the use of any information, apparatus, method, or process disclosed in this report may not infringe privately owned rights; or
- B. Assumes any liabilities with respect to the use of, or for damages resulting from the use of any information, apparatus, method, or process disclosed in this report.

As used in the above, "person acting on behalf of the Commission" includes any employee or contractor of the Commission, or employee of such contractor, to the extent that such employee or contractor of the Commission, or employee of such contractor prepares, disseminates, or provides access to, any information pursuant to his employment or contract with the Commission, or his employment with such contractor.

[The page contains extremely faint, illegible text, likely bleed-through from the reverse side of the document. The text is arranged in approximately 25 horizontal lines across the page.]

